

1 **Intracontinental deformation and volcanism in the**
2 **Hangai and Gobi-Altai Mountains in Mongolia:**
3 **Insights from a magnetotelluric multiscale 3-D**
4 **inversion**

5 J.S. Käuffl¹, A.V. Grayver¹, M.J. Comeau², A.V. Kuvshinov¹, M. Becken²,
J. Kamm²³, E. Batmagnai¹, S. Demberel⁴

¹*Institute of Geophysics, Department of Earth Sciences, ETH Zürich, Switzerland*

²*Institut für Geophysik, WWU Münster, Germany*

³*Geological Survey of Finland, Espoo, Finland*

⁴*Institute of Astronomy and Geophysics, Mongolian Academy of Sciences, Ulaanbaatar, Mongolia*

6 10 October 2019

7 **Summary**

8 Central Mongolia is a prominent region of intraplate volcanism and surface deformation. To
9 study these processes, which are poorly understood, we collected magnetotelluric data in the
10 Hangai and Gobi-Altai region in central Mongolia and derived the first three-dimensional
11 resistivity model of the crustal and upper mantle structure in this region.

12 The geologic history of this region is complex, resulting in features over a wide range
13 of spatial scales, which are coupled through a variety of geodynamic processes. Three-
14 dimensional imaging using magnetotellurics can resolve the distribution of electrical con-
15 ductivity within the Earth at scales ranging from tens of metres to hundreds of kilometres.
16 However, designing a survey which can probe various scales and running subsequent three-

17 dimensional inversions requires that multiple constraints imposed by the data acquisition
18 cost, logistical efforts and computational complexity are satisfied.

19 We present an approach to survey design, data acquisition, and inversion that aims to
20 bridge various spatial scales while keeping the required field work and computational costs
21 feasible. Magnetotelluric transfer functions were estimated for a $650 \times 400 \text{ km}^2$ grid, which
22 included measurements on an array with regular $50 \times 50 \text{ km}^2$ spacing and along several
23 profiles with a denser 5-15 km spacing. The use of telluric-only data loggers on these profiles
24 allowed for an efficient data acquisition with a high spatial resolution. A 3-D finite element
25 forward modelling and inversion code was used to obtain the resistivity model. Locally
26 refined unstructured hexahedral meshes allow for a multi-scale model parametrization and
27 accurate topography representation. The inversion process was split into four stages whereby
28 the result from each stage was used as input for the following stage, that included a finer
29 model parametrization and/or additional data (i.e. more stations, wider frequency range).

30 The final model reveals a detailed resistivity structure and fits the observed data well
31 across all periods and site locations, offering new insights into the subsurface structure of
32 central Mongolia. A prominent feature is a large low-resistivity zone detected in the upper
33 mantle that is attributed to partial melting within an asthenospheric upwelling that shallows
34 to a depth of 70 km, consistent with previous studies. The first 3-D model reveals the complex
35 geometry of the upwelling, which appears rooted below the Eastern Hangai Dome with a
36 second smaller upwelling southwest of the Hangai Dome.

37 Thanks to the multi-scale approach, the conductive signatures of late Cenozoic volcanic
38 zones and modern geothermal areas can be traced throughout the crust and lithosphere and
39 linked to the mantle upwelling. Other features of interest include well resolved, heterogeneous
40 low-resistivity zones in the lower crust, a highly resistive upper crust throughout the Hangai,
41 consistent with a cratonic block, and shallow, conductive sediments in the Valley of Lakes
42 south of the Hangai Dome. Furthermore, the conductive signatures of several major fault
43 systems were imaged, which accommodate the intracontinental deformation, mark terrane
44 boundaries, and host the mineralized zones of the Bayankhongor Ophiolite Belt.

45 **Key words:** Magnetotellurics, Inverse theory, Numerical modelling, Electrical proper-
46 ties, Asia, Structure of the Earth

47 1 INTRODUCTION

48 Located deep in the continental interior, far away from plate boundaries, central Mongolia is
49 a region of active intracontinental deformation (Calais et al. 2003; Walker et al. 2007, 2008)
50 and young Cenozoic volcanism (e.g. Barry et al. 2003; Ancuta et al. 2018). With the stable
51 Siberian Craton to the North, central Mongolia occupies the transition zone between the
52 North-South compressional regime of the India-Asia collision and the eastward extension
53 motion due to the Pacific subduction (Calais et al. 2003). This transition zone is dominated
54 by the Hangai Dome, a low relief, intracontinental plateau elevated up to 2 km above the
55 regional average (Cunningham 2001). It is bounded by large seismically active strike slip
56 faults, which experienced large (Magnitude > 8) intracontinental earthquakes in the last
57 century (Walker et al. 2007). Additionally, dispersed, low-volume, intraplate volcanism is
58 observed during the last 35 Ma throughout central Mongolia (Barry et al. 2003; Hunt et al.
59 2012; Ancuta et al. 2018).

60 The cause of the volcanism and the mechanism of the Hangai Dome uplift remain enig-
61 matic. In particular, the link between uplift and volcanism is an open topic of research. Some
62 authors argue for contemporaneous processes (e.g. Cunningham 2001; Sahagian et al. 2016),
63 whereas others claim that the uplift might have predated the volcanic activity (McDannell
64 et al. 2018).

65 Previous seismic and gravity studies of the region found a low velocity/low density
66 anomaly in the upper mantle below the Hangai confined to depths of 70 – 150 km (Priestley
67 et al. 2006; Tiberi et al. 2008), and a low shear-wave velocity anomaly that possibly extends
68 to a depth of more than 410 km (Chen et al. 2015). A thick crust (50 – 55 km) and a shal-
69 low (60 – 80 km) lithosphere-asthenosphere-boundary (LAB) was found by seismic studies
70 (Priestley et al. 2006; Petit et al. 2008) and is supported by the analysis of erupted xeno-
71 liths (Barry et al. 2003; Ionov 2002). Petrochemical analysis of erupted basalts and mantle

xenoliths estimates the melting source at depths of 70 to 150 km (Hunt et al. 2012; Barry et al. 2003), in good agreement with the depth of the LAB and the low velocity/low density anomalies.

This combined evidence is inconsistent with an earlier explanation for the intraplate volcanism: a deep-rooted mantle plume (Windley & Allen 1993). More recent explanations for the volcanism and uplift include crust-mantle interactions such as lithospheric thinning (due to delamination, convective removal, or edge-driven convection) or asthenospheric flow and dynamic topography (see Ancuta et al. 2018). However, a comprehensive explanation is still missing, partly due to the lack of detailed three-dimensional (3-D) images of the subsurface in the region. To obtain this information, we conducted a magnetotelluric (MT) survey in the Hangai and Gobi-Altai region from 2016 to 2018.

Geological and geodynamic processes, such as the intracontinental deformation in Mongolia and asthenospheric upwelling, happen at a wide range of spatial scales. This motivated us to design a MT survey and develop a 3-D inversion scheme that can consistently embrace and bridge multiple spatial scales.

In practice, any survey design is often limited by the cost of data acquisition and the required logistical effort. Because a uniform, dense grid of sites can be prohibitively expensive to collect, an attractive alternative is complementing a coarser, large-scale grid of sites with more densely spaced sites in regions of primary interest. Furthermore, the cost and logistical efforts of a survey can be significantly reduced when using the Telluric-Magnetotelluric (T-MT) method (Hermance & Thayer 1975), whereby the magnetic field is recorded only at a subset of locations (Iliceto & Santarato 1986; Yungul 1977; García & Jones 2005; Melosh et al. 2010; Campañà et al. 2014). From a methodological perspective, handling T-MT data requires only modest modifications of the data processing and inversion tools to take full advantage of simultaneously recording arrays (Egbert 2002). Both of these considerations were addressed during data analysis and inversion. For the three-dimensional interpretation of MT data collected at an observation grid of highly variable spacing, one needs an inversion strategy that provides sufficient flexibility in parametrizing the subsurface. This allows

100 varying lateral and vertical resolution lengths to be appropriately accounted for without
 101 using an excessive number of unknown model parameters, which would impose additional
 102 computational constraints and increase non-uniqueness.

103 In this paper we focus on the methodological side of the problem and present an ap-
 104 proach on how to bridge the different spatial scales in 3-D MT inversions, applied to the
 105 data collected in the Hangai and Gobi-Altai mountains in Mongolia. Implications regarding
 106 the Hangai uplift and volcanism, as well as regional geodynamics and geology, previously
 107 discussed by Comeau et al. (2018c) on the basis of a 2-D model from a subset of the data,
 108 are expand upon here with new insights from the 3-D resistivity model.

109 2 DATA

110 2.1 The magnetotelluric method

111 The MT method is a geophysical technique used to probe the conductivity structure of
 112 the Earth by using natural electromagnetic (EM) field variations (Rikitake 1948; Tikhonov
 113 1950; Cagniard 1953). The Earth's response to external excitation is described by frequency-
 114 dependent transfer functions (TF), which carry information about the electrical conductivity
 115 distribution. We work with the magnetotelluric impedance tensor \mathbf{Z} , which links horizontal
 116 electric and magnetic fields as:

$$\vec{E}_h(\omega, \vec{r}_l) = \mathbf{Z}(\omega, \vec{r}_l) \vec{H}_h(\omega, \vec{r}_l). \quad (1)$$

117 Here, ω is the angular frequency. $\vec{E}_h(\omega, \vec{r}_l) = (E_x, E_y)$ and $\vec{H}_h(\omega, \vec{r}_l) = (H_x, H_y)$ are the
 118 Fourier transforms of the horizontal components of the electric (E-) and magnetic (H-) fields
 119 at the location \vec{r}_l . Henceforth, the frequency dependence is implied and will be omitted for
 120 simplicity. H- and E-fields act as the input and output of the linear system described by the
 121 impedance

$$\mathbf{Z}(\vec{r}_l) = \begin{pmatrix} Z_{xx}(\vec{r}_l) & Z_{xy}(\vec{r}_l) \\ Z_{yx}(\vec{r}_l) & Z_{yy}(\vec{r}_l) \end{pmatrix}, \quad (2)$$

122 which is a second-order frequency dependent, complex-valued tensor. It carries the infor-
 123 mation about the 3-D electrical conductivity distribution σ in the earth. Instead of the
 124 conductivity, its inverse, the resistivity ($\rho = \sigma^{-1}$) can be used interchangeably. For each of
 125 the four tensor elements we can calculate the phase

$$\phi_{ij}(\vec{r}_l) = \tan^{-1}(Z_{ij}(\vec{r}_l)) \quad \text{with } i, j \in \{x, y\} \quad (3)$$

126 and apparent resistivity

$$\rho_{a,ij}(\vec{r}_l) = \frac{|Z_{ij}(\vec{r}_l)|^2}{\omega\mu_0}, \quad (4)$$

127 where μ_0 is the magnetic permeability of vacuum.

128 Conventionally, electric and magnetic fields are recorded at the same location \vec{r}_l . The
 129 T-MT method (Hermance & Thayer 1975) introduces an inter-site impedance, \mathbf{Z}_i , defined
 130 as

$$\vec{E}_h(\vec{r}_l) = \mathbf{Z}_i(\vec{r}_l, \vec{r}_b) \vec{H}_h(\vec{r}_b), \quad (5)$$

131 whereby \mathbf{Z}_i is calculated with the E-field measured at the location \vec{r}_l and the H-field measured
 132 at the location \vec{r}_b (denoted as base site). Recently, Comeau et al. (2018c) inverted a single
 133 profile of MT data across Mongolia and showed that using \mathbf{Z}_i does not compromise resolution
 134 and leads to reliable subsurface images. In fact, this approach can further help in suppressing
 135 local noise (Egbert 2002; Campányà et al. 2014).

136 2.2 Data acquisition

137 During three field surveys in the years 2016 to 2018, data was collected on a 650×400 km²
 138 grid (see Fig. 1 and Table 1 for abbreviations of geographic features). The survey covers
 139 the Hangai Mountains, a part of the Gobi-Altai mountain range, the Valley of Lakes, and
 140 surrounding areas. For the inversion model presented here, we use transfer functions from
 141 272 unique locations with 97 sites laid out on a quasi-uniform grid with 50 km spacing and
 142 175 sites along four profiles (P2, P3, P4, and P6 in Fig. 1) with a spacing of 5 to 15 km.
 143 Additional sites are located in the Tariat volcanic field (TV, Comeau et al. 2018a) and the
 144 Tsenkher geothermal area (TGT).

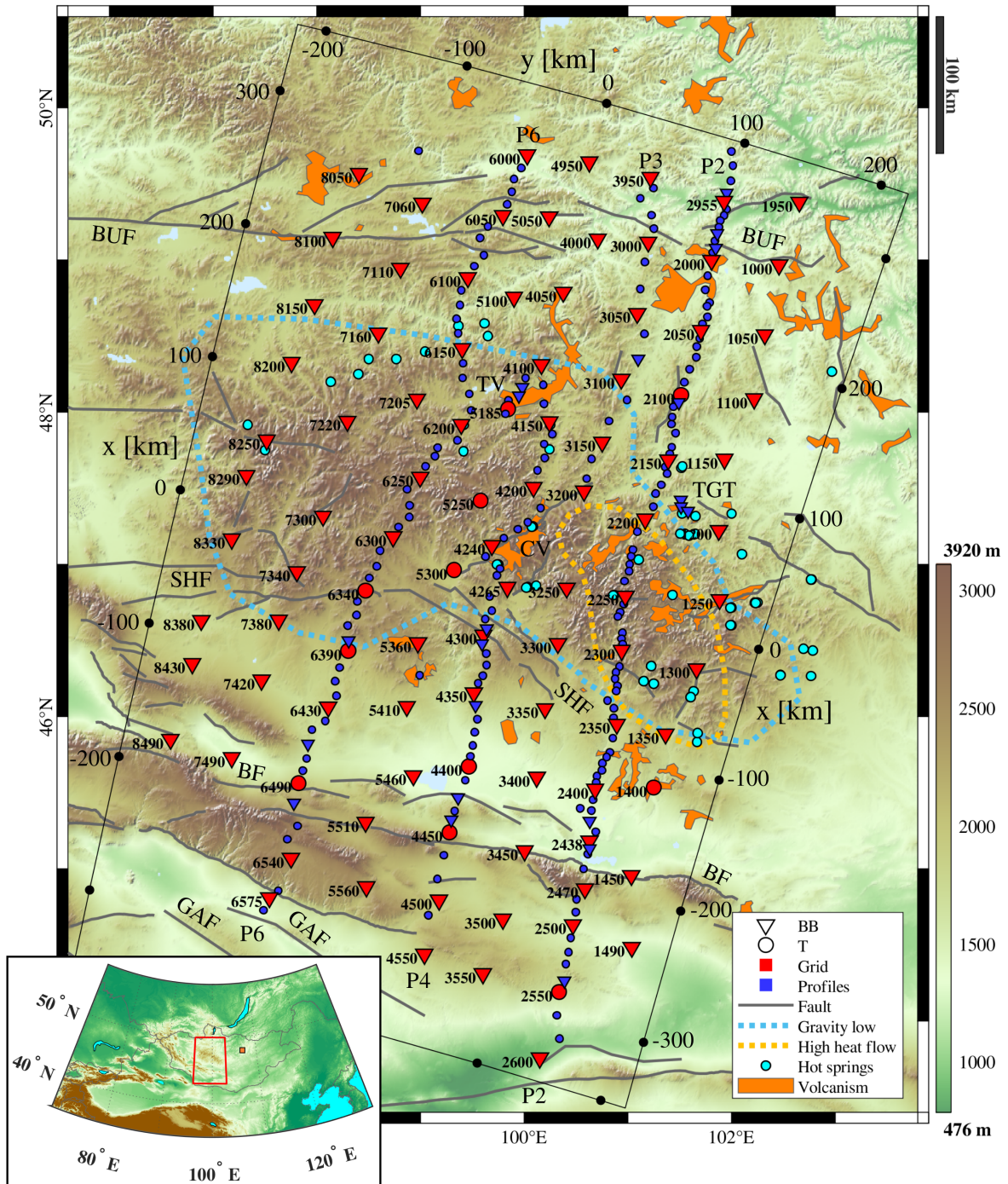


Figure 1. Topographic map with installed sites in central Mongolia. The location in central Asia is indicated in the smaller inset in the lower left. See Table 1 for abbreviations. The symbol indicates the type of instrument used. Red color indicates the grid sites and blue color the others. The grid sites are indicated with their numeric designation. Grey lines mark major fault systems (Walker et al. 2008; Styron 2018), the dotted blue line indicates the -250 mGal Bouguer anomaly (Tiberi et al. 2008), the dotted orange line indicates the 90 mW/m² high heat flow anomaly, light blue circles mark hot spring locations (Oyuntsetseg et al. 2015; Ganbat & Demberel 2010), and the orange patches designate Cenozoic volcanic provinces (Ancuta et al. 2018). The black frame around the survey area indicates the rotated local cartesian coordinate system used for the 3-D inversion.

AS:	Asthenosphere
BF:	Bogd fault
BUF:	Bulnay fault
CV:	Chuluut volcanic zone
EHC:	East Hangai conductor
GAC:	Gobi-Altai conductor
GAF:	Gobi-Altai fault
HB:	Hangai block
LAB:	Lithosphere-Asthenosphere boundary
NHC:	North Hangai conductor
SHC:	South Hangai conductor
SHF:	South Hangai fault
TV:	Tariat volcanic zone
TGT:	Tsenkher geothermal area
VL:	Valley of Lakes
VLR:	Valley of Lakes resistor
WHC:	West Hangai conductor

Table 1. Table of abbreviations used throughout the text and in figures.

145 We employed two types of instruments: broadband (B) and telluric-only (T). Generally,
 146 B-instruments were used for the grid sites, while T-instruments were installed on the pro-
 147 files. For some of the sites we had to deviate from this scheme due to data quality issues
 148 and instrument availability during the measurement campaign. All instruments recorded
 149 the horizontal electric field (60 m dipole length with either silver-chloride or lead-chloride
 150 electrodes). B-sites additionally recorded all three components of the magnetic field. At B-
 151 locations, Metronix ADU-07e and SPAM Mk4 data loggers with Metronix induction coils
 152 (MFS-06, MFS-10, MFS-11) were used. Recording was done for three to five days with a
 153 sampling frequency of 512 Hz. Additional long period instruments (Geomag Fluxgate and
 154 EarthData data loggers) were installed at 14 locations along profiles P2 and P4. Recording
 155 time was between 10 and 32 days with a sampling frequency of 2 Hz. The telluric instruments
 156 were designed by the University of Münster for fast and easy deployment, thus allowing for

157 efficient data collection with dense site spacing. They recorded with a sampling frequency
 158 of 512 Hz for a duration of twelve hours to three days.

159 2.3 Transfer functions

160 Impedance tensors were estimated with a robust processing scheme, using the M-estimator
 161 (Egbert & Booker 1986) and a minimal covariance determinant method (Rousseeuw 1984;
 162 Platz & Weckmann 2019) to improve long period TF when only a few time windows are
 163 available (Harpering 2018). To maximise the quality and period range of TF, processing
 164 parameters (such as time window selection, bi-coherence threshold values, single site or
 165 remote referencing, base site selection for inter-site impedances) were chosen individually
 166 for each site. After processing, we obtained a set of 272 TF of high quality in the period
 167 range from 0.0078 s to 3000 s at most sites with periods going up to 8000 s and 24000 s
 168 for some broad-band and long-period sites, respectively. Fig. 2 shows a representative set of
 169 transfer functions at six locations.

170 Generally, we see that data north of the South Hangai fault (SHF; see 4150BL, 2240T,
 171 and 6120T in Fig. 2) exhibit much less spatial variability compared to the sites south of
 172 the SHF (1450B in Fig. 2 as well as 2350BL and 4350BL in Fig. 5), which show a very
 173 different behaviour. Overall, the data is affected by galvanic distortions. For instance, three
 174 of the four sites shown in Fig. 2 (4150BL, 2240T, and 6120T) exhibit a static shift effect
 175 (large differences of ρ_{xy} and ρ_{yx} between the sites but with similarly-shaped curves, as well
 176 as similar ϕ_{xy} and ϕ_{yx}). Berdichevsky et al. (1980) showed that the static shift effect follows
 177 a log-normal distribution and an unbiased regional 1-D impedance can be obtained with the
 178 geometric mean of the determinant of \mathbf{Z} . In this paper, the sum of the squared impedance
 179 elements (SSQ-impedance)

$$Z_{ssq}(\vec{r}_l) = \sqrt{\frac{Z_{xx}(\vec{r}_l)^2 + Z_{xy}(\vec{r}_l)^2 + Z_{yx}(\vec{r}_l)^2 + Z_{yy}(\vec{r}_l)^2}{2}} \quad (6)$$

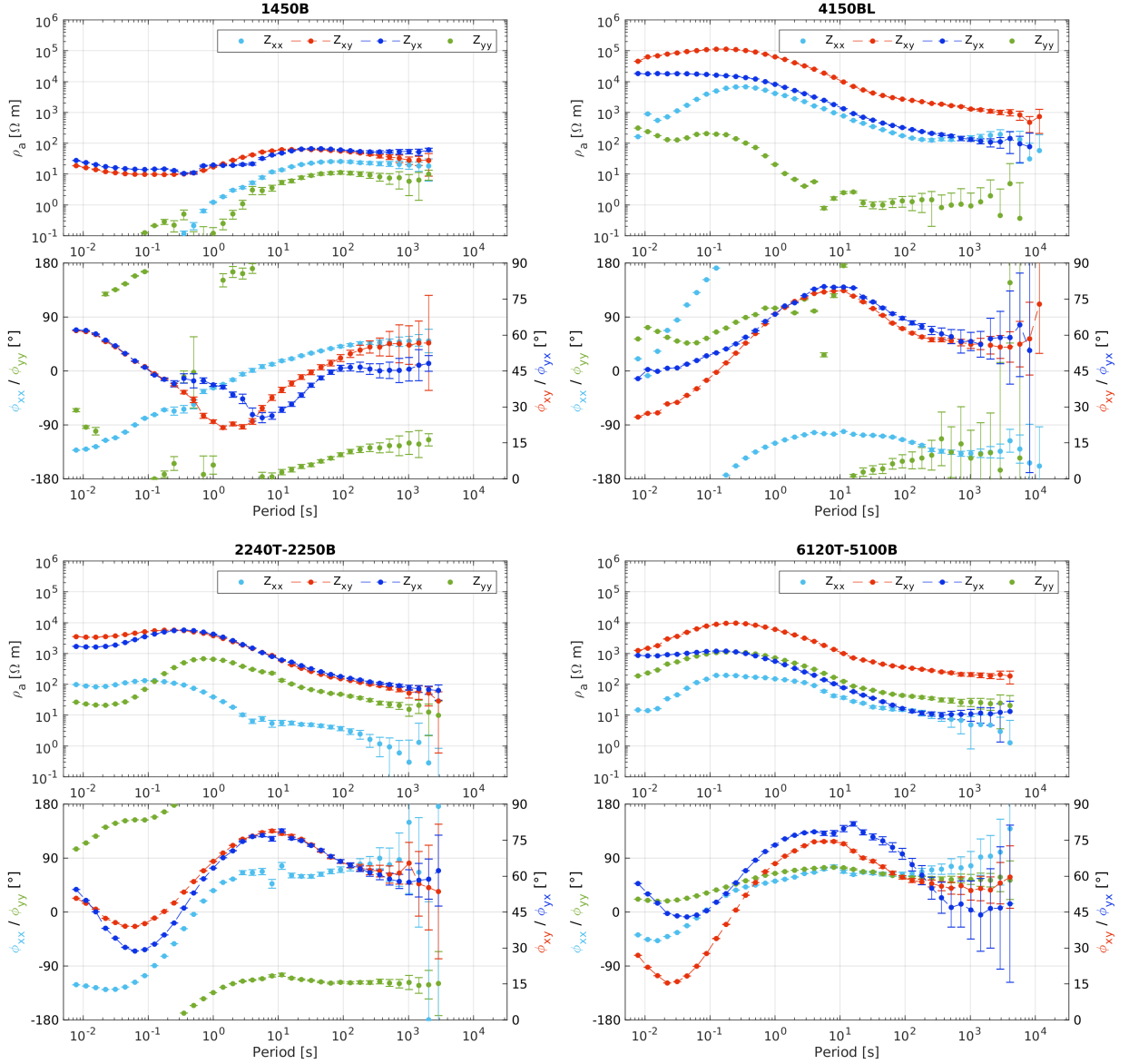


Figure 2. Apparent resistivity and phase curves at six representative sites. The off-diagonal phases (ϕ_{xy} and ϕ_{yx}) are shifted to the first quadrant for better visibility. 1450B is a broadband site, 4150BL is a broadband and long-period site, 2240T and 6120T are telluric sites with their respective base sites given in the plot titles.

180 for each location \vec{r}_l is used to obtain a regional 1-D impedance,

$$\bar{Z}_{1-D} = \sqrt[N]{\prod_{l=1}^N Z_{ssq}(\vec{r}_l)}, \quad (7)$$

181 where N denotes the total count of locations used. Compared to the impedance determi-
 182 nant, it is less affected by a downward bias due to distortion (Rung-Arunwan et al. 2016).

183 The apparent resistivities and phases obtained from the SSQ-impedances for the grid sites

184 are shown in Fig. 3a for periods $T > 1$ s. Apparent resistivities for northern sites vary over
 185 two orders of magnitude, whereas the phase shows smaller variability, especially for periods
 186 $T > 10$ s. We conclude that the 1-D impedance calculated from averaged northern SSQ-
 187 impedances provides a reasonable representation of the regional 1-D conductivity structure.
 188 Southern sites, on the other hand, show a large variability in both ρ_a and ϕ curves over the
 189 entire period range, indicating a substantially inhomogeneous regional conductivity distri-
 190 bution. As a result, the southern regional 1-D impedance is likely not representative of a
 191 regional conductivity structure.

192 Further, Fig. 3b shows the real part of the C-response,

$$C = -\frac{\bar{Z}_{1-D}}{i\omega\mu_0}, \quad (8)$$

193 calculated for both regional 1-D impedances. It represents the depth of the “center of mass”
 194 of induced currents for a given period (Weidelt 1972) and can be used as a proxy for the
 195 penetration depth. Starting with a penetration depth of 4-15 km at 1 s, the penetration
 196 depth increases to 200 km at the period of 4096 s.

197 We performed a dimensionality analysis by calculating the phase tensor strike angle θ and
 198 the normalized skew angle Ψ (Booker 2014). The polar histograms of θ in Fig. 4 reveal that
 199 there are two clear strike directions for periods $T > 10$ s, namely $\approx 15^\circ$ and -75° (clockwise
 200 from magnetic North). With a normalized skew angle of $\Psi > 6^\circ$ over a wide period range
 201 at the majority of the sites (see the supplementary material, Sec. S1), the collected data
 202 shows a significant influence of 3-D effects (Booker 2014). Thus a 3-D inversion is indeed
 203 indispensable to retrieve all information from the dataset.

204 As was previously shown by Tietze & Ritter (2013), when a predominant geological strike
 205 direction exists, it is advantageous to rotate the impedance tensor even for 3-D inversion,
 206 thereby improving inversion convergence and reducing modelling errors. Therefore, we ro-
 207 tated the impedance tensors by 15° counter-clockwise, thus aligning the principal axes not
 208 only with the strike directions but also the profile directions. An additional benefit of the
 209 rotation is the correction of out of quadrant off-diagonal phases, that can be observed at

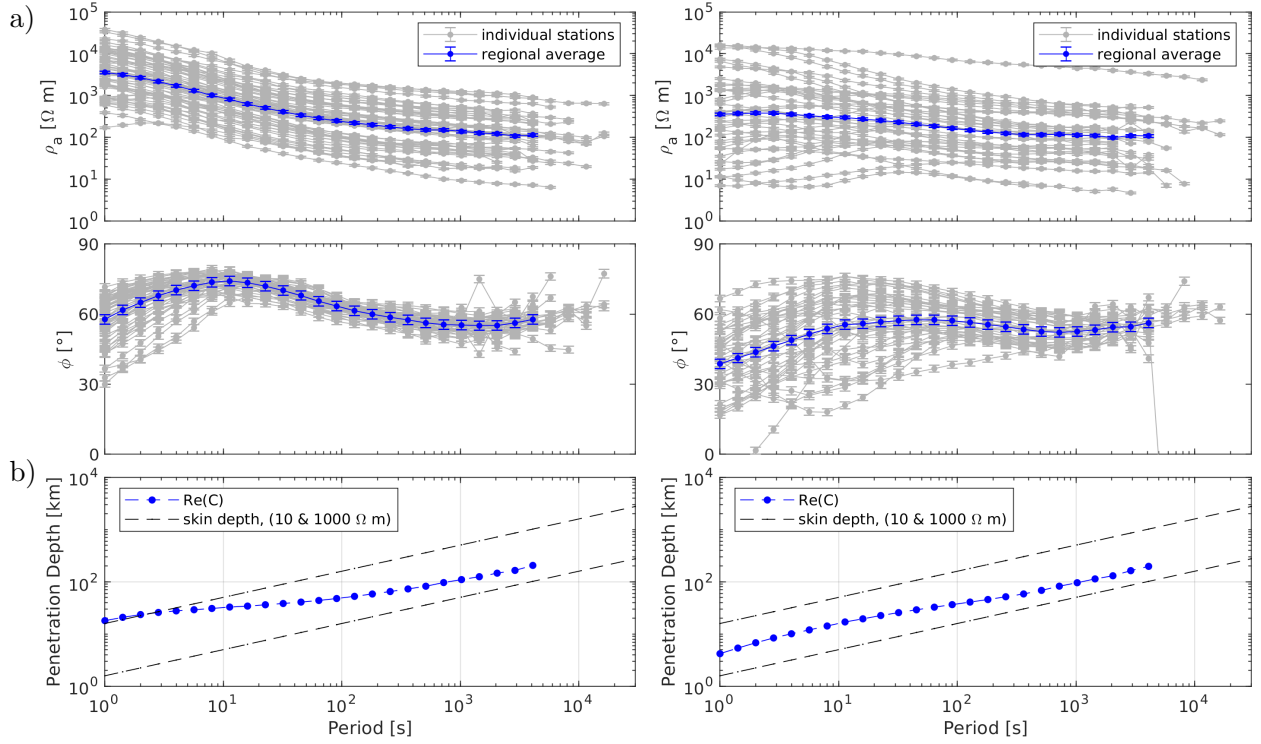


Figure 3. SSQ-impedances and penetration depths estimated from grid site data north (left) and south (right) of the SHF (see Fig. 1). a) ρ_a and ϕ calculated from the SSQ-impedance of each individual site (grey) and from the regional 1-D impedance (Eq. 7; blue). b) The real part of the C-response for both regional 1-D averages, a measure for the penetration depth, together with the skin depths for a homogeneous half space of 10 and 1000 Ωm .

210 some of the sites. This is shown in Fig. 5 for two sites, 2350BL and 4350BL. For both sites
 211 $\rho_{xy} > \rho_{yx}$, indicating East-West oriented low resistivity anomalies. A phase tensor analysis
 212 of these sites reveals strong 3-D influences with a normalized skew angle of $\psi > 6^\circ$ in the
 213 period range of 0.1–10 s, indicating that shallow (less than 10 km) 3-D anomalies are most
 214 likely the cause of these out of quadrant phases. After rotating the impedance tensor by 15°
 215 counter-clockwise from magnetic North, phases remain in their respective quadrants for the
 216 entire period range.

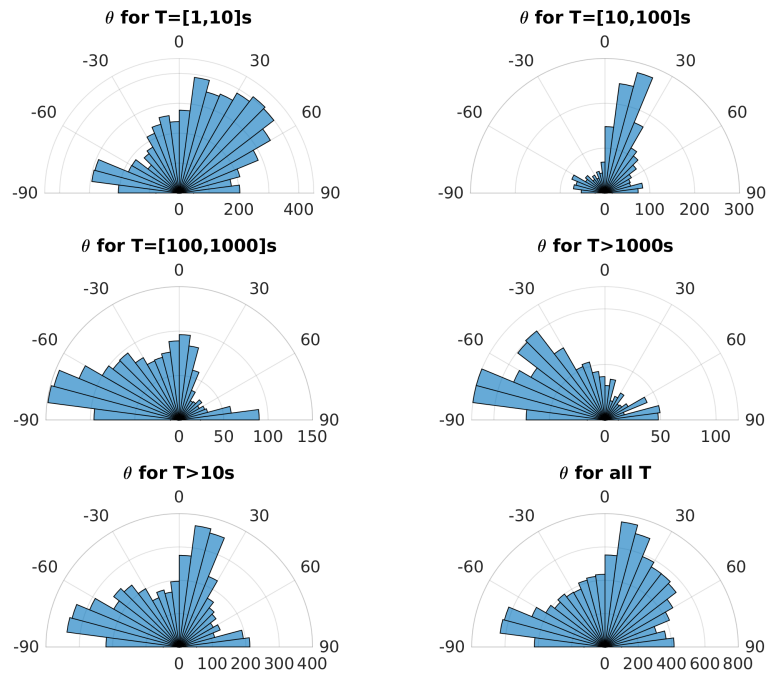


Figure 4. Polar histograms of the phase tensor strike angle θ (clockwise from magnetic North) for different period bands. From 10 s to 100 s a clear strike direction of 15° can be seen, whereas longer periods show a strike of -75° .

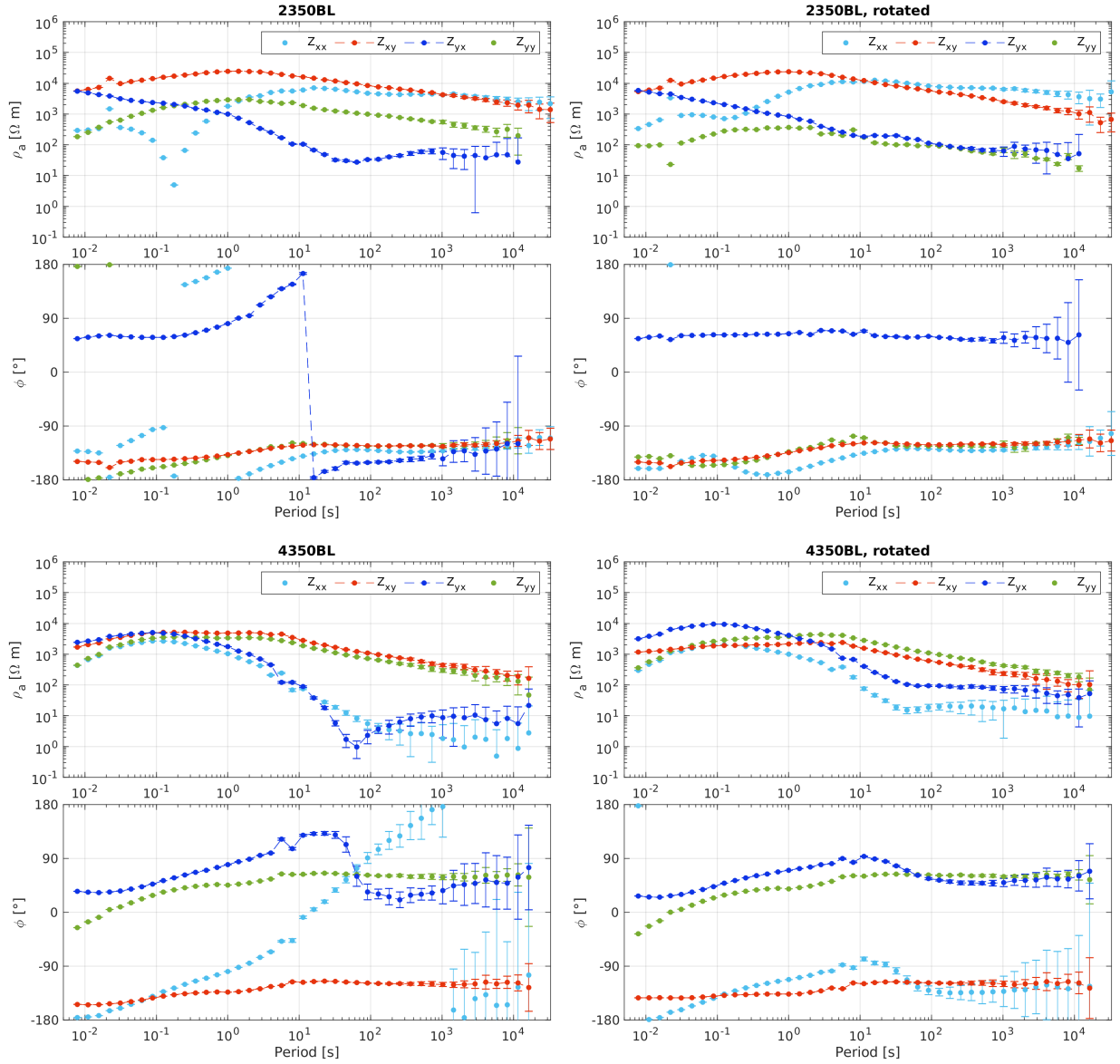


Figure 5. Sounding curves for the sites 4350BL and 2350BL, left: coordinate system oriented along magnetic North, right: rotated coordinate system (15° counterclockwise from magnetic North). After rotation, previously out of quadrant phases remain in their respective quadrants over the entire period range.

3 METHODOLOGY

Owing to the wide frequency range of MT source signals (10^{-4} to $\approx 10^5$ s), together with the typical electrical resistivity range of the Earth (0.1 to $10^5 \Omega\text{m}$), the inversion of MT data can efficiently resolve electrical resistivity variations in a wide range of spatial scales from tens of metres to hundreds of kilometres. MT has been used to successfully image shallow volcanic and geothermal systems with extents ≈ 10 km with lateral resolution of less than one kilometer (e.g. Heise et al. 2007; Bertrand et al. 2012; Muñoz 2014; Hill et al. 2015; Peacock et al. 2016; Usui et al. 2016; Samrock et al. 2018). At regional scales, MT is commonly used to image crustal and lithospheric structures with a resolution between 1-10 km (e.g. Khoza et al. 2013; Tietze & Ritter 2013; Nieuwenhuis et al. 2014; Cherevatova et al. 2015; Robertson et al. 2017; Xu et al. 2019). In recent years, models obtained by inverting continental scale surveys have appeared with a lateral resolution of tens of kilometres, including the USArray, AusLAMP, and SinoProbe projects (Meqbel et al. 2014; Yang et al. 2015; Robertson et al. 2016; Dong et al. 2016; Murphy & Egbert 2017). However, these surveys rarely bridge multiple spatial scales. The necessary methodological adaptations to the inversion process are outlined below.

3.1 Forward modelling

Electromagnetic fields in a 3-D medium are calculated by solving the following equation

$$\nabla \times (\mu_0^{-1} \nabla \times \vec{E}) + i\omega\sigma\vec{E} = 0 \quad \text{in } \Omega. \quad (9)$$

Here, $\Omega \subseteq R^3$ is the modelling domain, \vec{E} the electric field vector and σ the electrical conductivity. Further, the inhomogeneous Dirichlet boundary conditions,

$$\vec{E} = \vec{E}_0 \quad \text{on } \partial\Omega, \quad (10)$$

are applied, where \vec{E}_0 results from the solution of 2-D Maxwell's equations on the boundaries. The magnetic field \vec{H} is obtained by virtue of Faraday's law. Solutions for two orthogonal source polarisations are computed to be able to derive the full impedance tensor.

The 3-D finite element code GoFEM (Grayver & Kolev 2015) was used to discretize Eq.

(9) and find a numerical solution. It is based on the finite-element library deal.II (Alzetta et al. 2018) and uses PETSc (Balay et al. 2018) with METIS (Karypis & Kumar 1999) for distributed linear algebra and mesh partitioning, respectively. The resulting system of linear equations was solved with a parallel version of the iterative FGMRES solver and auxiliary-space multigrid preconditioner as described in detail by Grayver & Kolev (2015). To improve accuracy of the numerical solutions and to discretize topography accurately, we used locally refined non-conforming hexahedral meshes, as described in Section 3.3.

3.2 Inversion

To obtain the electrical conductivity distribution that explains the measured data we solve a non-linear inverse problem (e.g. Dmitriev et al. 1976; Aster et al. 2018) by minimising the objective function

$$\Phi(\mathbf{m}) = \frac{1}{2}\Phi_d(\mathbf{d}, \mathbf{m}) + \frac{\alpha}{2}\Phi_m(\mathbf{m}), \quad (11)$$

which consists of a data term Φ_d and a model term Φ_m , balanced by the regularization parameter α . \mathbf{m} is a vector of the unknown model parameters (i.e. the electrical conductivity) and \mathbf{d} the data vector, containing the TF. For this study we used the real and imaginary parts of either the regional 1-D impedance (Eq. 7, for a 1-D inversion) or all four impedance tensor components (Eq. 2, for a 3-D inversion). No additional static-shift correction was done.

The data term

$$\Phi_d(\mathbf{m}, \mathbf{d}) = \|(f(\mathbf{m}) - \mathbf{d})\|_{\mathbf{C}_d^{-1}}^2, \quad (12)$$

contains the difference between the observed and the modelled TFs, which are obtained from the forward modelling operator $f(\mathbf{m})$ given a model \mathbf{m} . The data is weighted by the data covariances \mathbf{C}_d , given here by a diagonal matrix containing the data variance δZ^2 .

Because of strong galvanic distortions, a relative error e was applied row-wise to the absolute of \mathbf{Z} at each period, giving data variances

$$\delta Z_{jx}^2 = \delta Z_{jy}^2 = (e \cdot \max(|Z_{jx}|, |Z_{jy}|))^2 \quad \text{with } j \in \{x, y\}. \quad (13)$$

264 To prevent imbalance between grid and profile sites, we found that an error $e = 0.03$ for the
 265 grid and $e = 0.05$ for the profiles allows us to achieve a uniform fit for all sites. Thereby, TF
 266 at the profile sites are slightly down-weighted in comparison to TF from the grid sites.

267 The model or regularization term

$$\Phi_m(\mathbf{m}) = \|R(\mathbf{m})\|^2 \quad (14)$$

268 is given by the roughness operator $R(\vec{m})$, aimed to stabilize the ill-posed and generally non-
 269 unique inverse problem (Tikhonov 1963). No reference model is used in the regularization
 270 term. Thereby, the roughness of the model (characterized by the conductivity jumps across
 271 the adjacent cells) is minimized.

272 GoFEM uses the Gauss-Newton method to minimize the functional in Eq. (11) (Grayver
 273 2015). A unit step length for the model update is used. While this can lead to an increase
 274 in Φ , it usually allows the inversion to escape a local minimum.

275 The regularization parameter

$$\alpha = \gamma \frac{\|\mathbf{J}^T \mathbf{C}_d^{-1} \mathbf{J}\|_2}{\|\mathbf{R}\|_2} \quad (15)$$

276 is determined for each iteration step by the ratio of the L_2 -norms of the weighted approx-
 277 imate Hessian $\mathbf{J}^T \mathbf{C}_d^{-1} \mathbf{J}$ and the regularization matrix \mathbf{R} . \mathbf{J} denotes the Jacobian of $f(\mathbf{m})$.
 278 The scaling factor $\gamma \in (0, 1]$ is a user-determined parameter. We adopted a cooling regular-
 279 ization by gradually decreasing the regularization strength through smaller γ . In practice,
 280 this approach facilitates the recovery of the dominating large-scale conductivity variations
 281 followed by smaller structures later during the inversion process.

282 3.3 Model discretization

283 The modelling domain Ω is discretized using hexahedral elements. To ensure numerical
 284 accuracy and to decrease the ambiguity of the non-unique problem, we use locally refined
 285 meshes. As outlined by Käüfl et al. (2018), an initially coarse mesh is locally refined within
 286 the area of interest and then transformed to conform to the topography.

287 The mesh used in this study has a size of $4000 \times 4000 \times 3000 \text{ km}^3$ and consists of 6800 cells

288 initially. The subsequent refinements were guided by the penetration depth inferred from the
289 C-responses (Fig. 3b). After two refinements at the air-ground interface, three refinements in
290 the central area of interest, and three refinements around site locations, the mesh consists of
291 215000 cells. Within the survey area, cell diameters range from 4.7 km close to the MT sites
292 to 19 km in the upper mantle down to a depth of 200 km. At greater depths and outside the
293 survey area, cells increase gradually towards the domain boundary. Finally, the meshes are
294 adjusted to the topography (elevation data provided by NASA JPL 2013) and cells in the
295 air are assigned a resistivity of $10^9 \Omega\text{m}$. The resulting mesh is shown in Fig. 6a. A second
296 finer mesh is obtained by further refinement, resulting in 321000 cells with a minimal cell
297 diameter of 2.4 km near sites (Fig. 6b). This represents our inverse model parametrization.

298 As is shown by Joshi et al. (2004) and Grayver (2015), it may be advantageous to decou-
299 ple forward/adjoint and inverse model parametrizations. Specifically, we use an additional
300 refinement step in a 5 km radius around site locations for forward and adjoint solutions in
301 order to better represent local topography and increase numerical accuracy for higher fre-
302 quencies. A coarser mesh for the targeted parameter (that is, electrical conductivity) reduces
303 computational cost and decrease ambiguity, thereby making the problem less ill-posed. Note
304 that due to hierarchical relation between both forward/adjoint and inverse grids, we avoid
305 any interpolation and simply assign conductivity from the coarser inverse grid cells to refined
306 forward/adjoint grid cells.

307 Following the arguments from Section 2.3, we perform the inversion in a local Cartesian
308 coordinate system with x- and y-axes rotated 15° clockwise from North and East respectively.
309 The z-axis points downward. The origin corresponds to the center of the survey grid at
310 47°N , 99.5°E (sea level). All geographic coordinates are transformed into the modelling
311 domain by referencing their UTM coordinates (zone 47, WGS84 reference ellipsoid) to 47°N ,
312 99.5°E followed by a rotation around the origin. The resulting cartesian coordinate system
313 is indicated in Fig. 1.

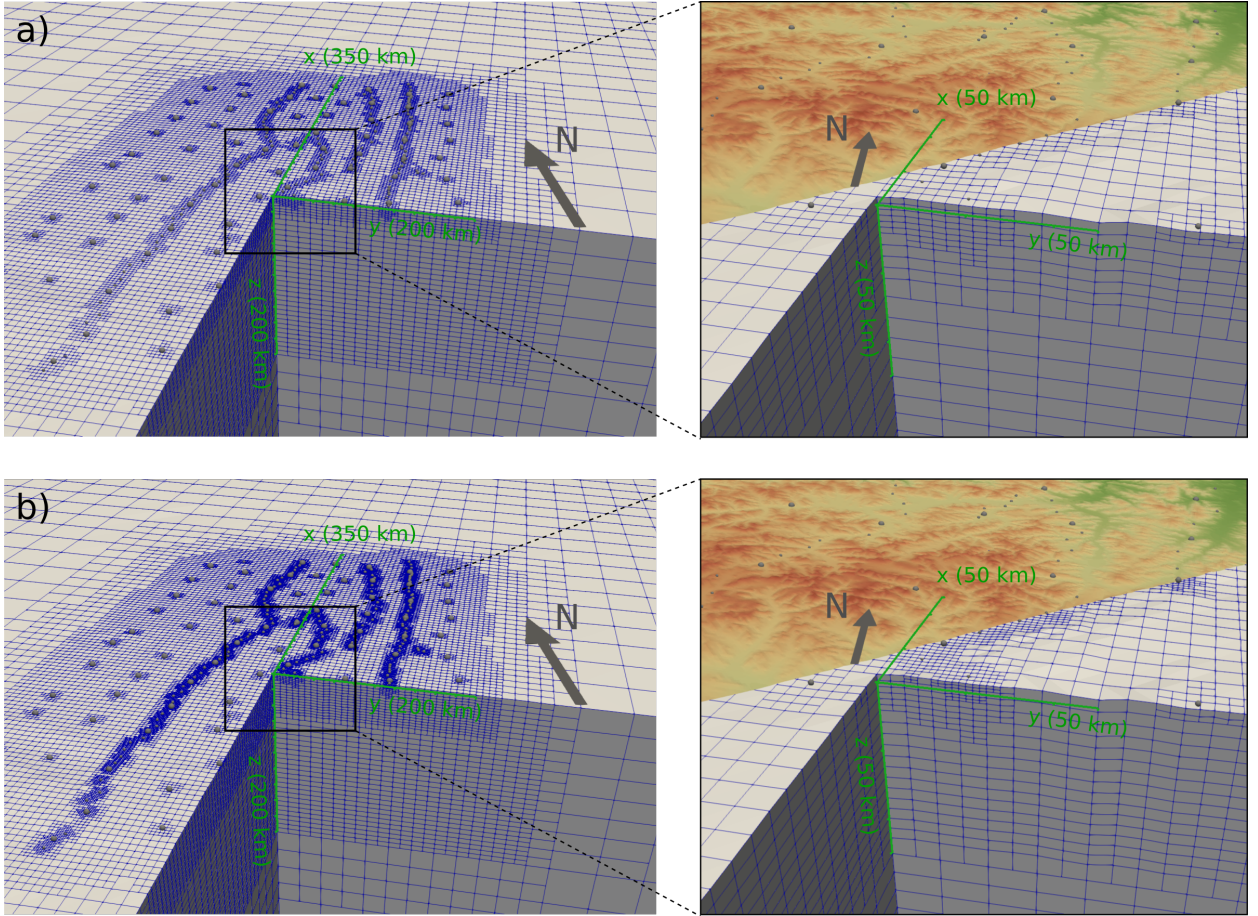


Figure 6. Cutaway view of the coarse (a) and fine (b) inversion meshes as well as a zoomed-in view of the central part. Local Cartesian axes (shown in green) are rotated by 15° clockwise from magnetic North.

314 3.4 Inversion methodology

315 We designed a multi-stage approach for inverting the data as shown in the flow-chart Fig.
 316 7. We start by inverting the regionally averaged 1-D impedance \bar{Z}_{1-D} , followed by the 3-D
 317 inversion with increasing number of sites and a wider period band. As illustrated in Fig. 7,
 318 the final result of each stage is used as the starting model for the subsequent stage, which
 319 is done with a finer mesh and more data.

320 The objective function (eq. 11) has multiple minima. To prevent the inversion from
 321 getting trapped in a local minimum that may not correspond to a geologically plausible
 322 model, the choice of the starting model is crucial. Rung-Arunwan et al. (2016) proposed
 323 to use a 1-D model derived from the regional 1-D impedance (eq. 7) as a starting model.

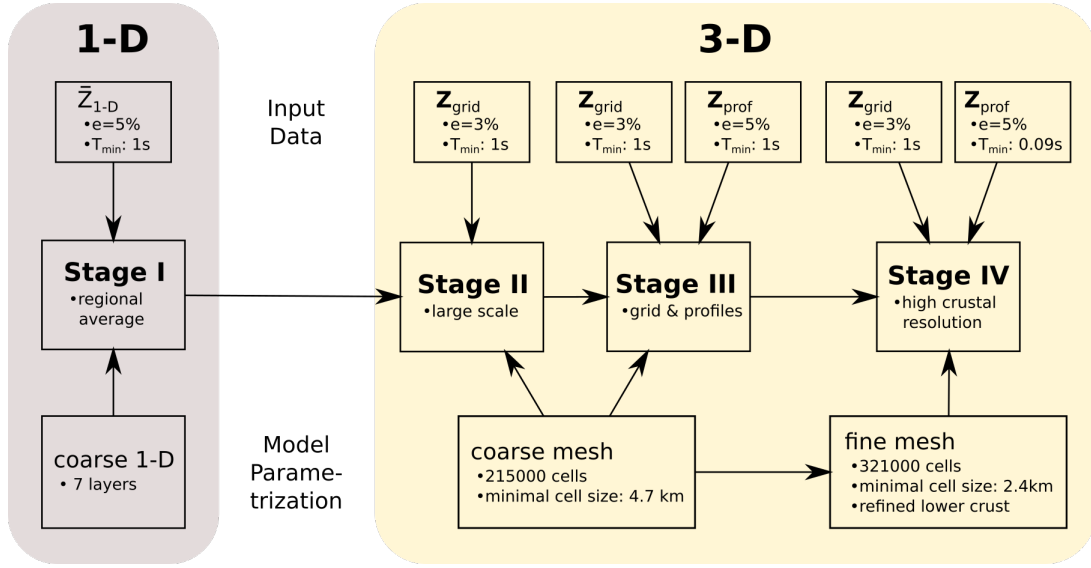


Figure 7. Flow chart of the inversion process, consisting of four stages with different model parametrizations and input data. \bar{Z}_{1-D} is the regionally averaged 1-D impedance (eq. 7), while Z_{grid} and Z_{prof} indicate the 2×2 impedance tensors from grid and profile sites (see Fig. 1). e corresponds to the assigned data error (eq. 13) and the shortest period is denoted by T_{min} .

324 To calculate the regional average, we used a stochastic inversion algorithm based on the
 325 Covariance Matrix Adaption Evolution Strategy (CMAES, see Grayver & Kuvshinov 2016),
 326 followed by a Markov chain Monte Carlo (MCMC) walk to evaluate its uncertainty. The
 327 obtained 1-D conductivity model is then used as an initial model for the 3-D inversion in
 328 Stage II.

329 For Stage II, only the 2×2 impedance tensors (with $T > 1$ s) from quasi uniformly
 330 spaced grid sites Z_{grid} (red sites in Fig. 1) are inverted. The resulting model is then passed
 331 on to Stage III, where 2×2 impedance data from the profile sites Z_{prof} (blue sites in Fig.
 332 1) are added, most of which are telluric sites with inter-site impedance tensors estimated
 333 using the H-field from a nearby full MT station. Based on the result from this step, the
 334 final inversion step is performed with the finer mesh (further refinement in the lower crust)
 335 and impedances at shorter periods ($T > 0.09$ s). We found that this approach not only
 336 reduces computational costs compared to running the inversion on the fine mesh directly,
 337 but it also improves convergence significantly and enables the imaging of large and small
 338 scale structures within a single model.

339 **4 RESULTS**340 **4.1 Stage I: regional 1-D models**

341 As outlined in Section 3.4, the regional 1-D impedances for sites north and south of the
 342 SHF (see Fig. 3) were inverted to obtain 1-D conductivity models (see Fig. 8). The model
 343 consists of seven homogeneous layers, consistent with the depth discretization of the 3-D
 344 mesh. The best fit models agree with the data well. As outlined in Section 2.3, \bar{Z}_{1-D} derived
 345 from the southern sites is likely not representative of a regional conductivity structure. As a
 346 result, we used the 1-D model derived from the northern sites to be the starting model for
 347 the subsequent 3-D inversion of the whole region.

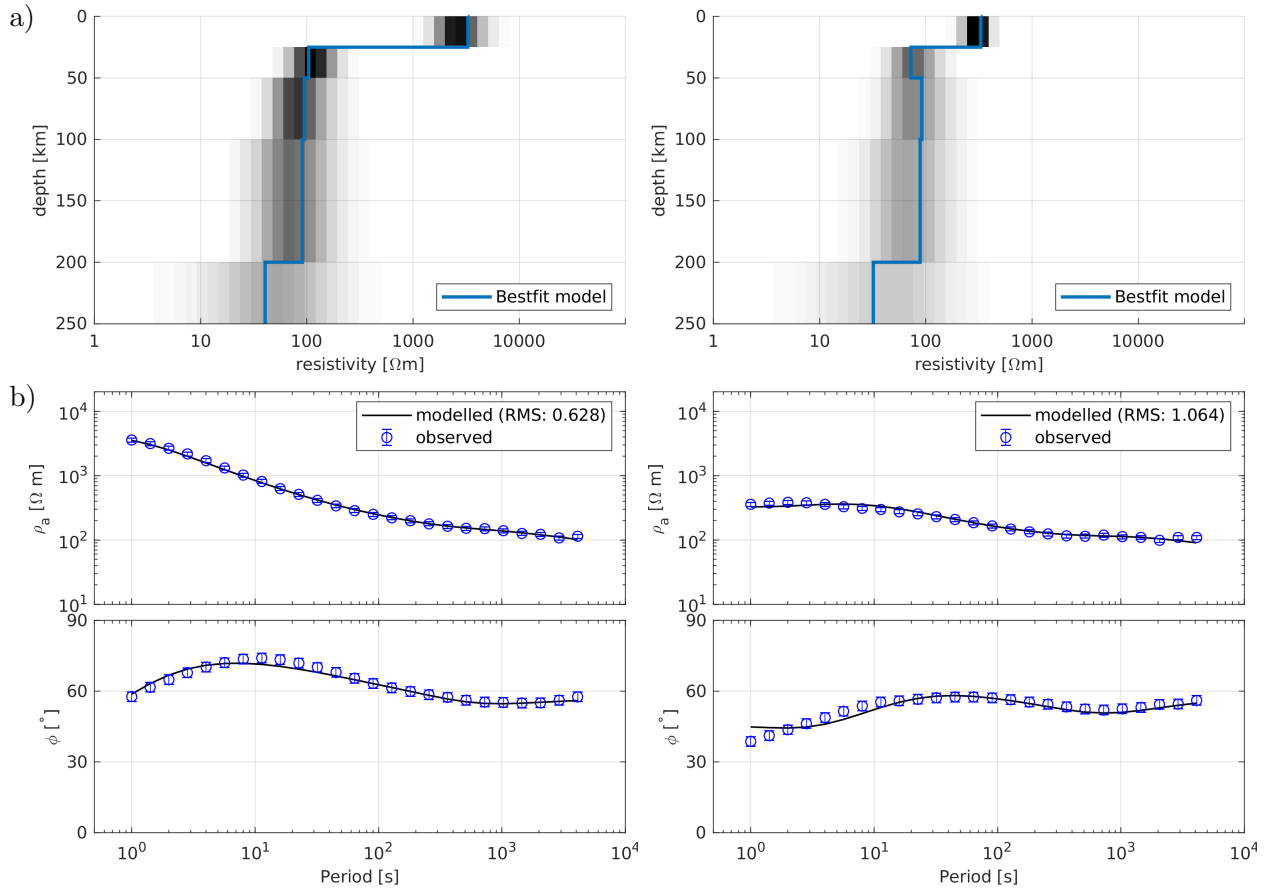


Figure 8. a) Regional 1-D conductivity models (blue), together with a distribution of equivalent models (grey shaded areas) for sites north (left panels) and south (right panels) of the SHF. b) Their data fit for sites north (left panels) and south (right panels) of the SHF.

4.2 Stage II: 3-D large-scale inversion

For this stage, only data from the grid sites (50 km nominal spacing) were inverted. Fig. 9 shows the progressive reduction of the data misfit (as defined by a root-mean squared misfit, RMS) and regularization parameter for each iteration step. As discussed in Section 3.2, the regularization parameter was decreased over the course of the inversion to permit more structure in the model. Starting from an RMS value of 43.1 using the initial 1-D model (see Section 4.1 and Fig. 8), the inversion achieved an RMS value of 2.65 after 19 iterations. Fig. 9a) shows an increase in the misfit for four out of the 19 iterations, indicating an escape from a local minimum or an overshoot, yet this did not prevent the inversion from converging. A continuation with even lower regularization resulted in negligible misfit reductions ($< 3\%$ per iteration) and therefore the inversion was terminated.

The best-fit model (model S2) is shown in Figs 10 and 11 (see Table 1 for abbreviations of geographic and model features). The upper crust is characterised by the resistive Hangai cratonic block (HB) north of the SHF and the very heterogeneous and generally conductive Valley of Lakes (VL) south of the SHF. The Bogd fault (BF) can be traced as a strong conductor. In contrast, the Bulnay and Gobi-Altai Faults (BUF and GAF respectively) are not clearly imaged. At depths of 30 to 35 km below the Hangai, there is an abrupt drop in resistivity of three to four orders of magnitude, most likely indicating a transition to the ductile lower crust. The lower part of the crust (35-50 km) is a heterogeneous conductor, labelled as North, East, South, and West Hangai Conductor (NHC, EHC, SHC, and WHC, respectively). The Valley of Lakes on the other hand is underlain by a resistor (VLR). In the upper mantle (below 50 km) and above the Asthenosphere (AS), resistivities are again higher, except for the SHC and EHC. They extend vertically from the lower crust to the AS.

The single RMS value of the best fitting model is not sufficient to judge its quality (Tietze & Ritter 2013; Miensopust 2017). Instead, the results were evaluated based on the convergence (see Fig. 9), data fit distribution over periods and site locations, as well as histograms of the residuals. Fig. 12 gives a detailed breakdown of the data fit. RMS values

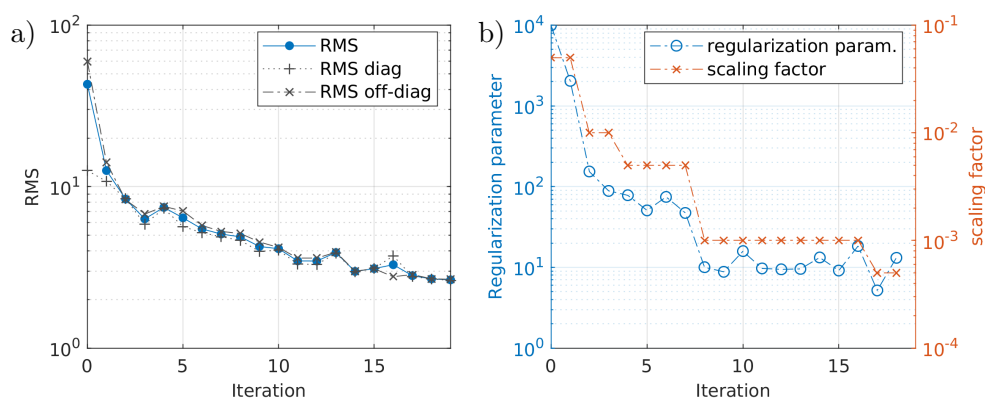


Figure 9. Progression of the RMS value (a) and regularization (see eq. 15) parameters (b) during Stage II of the inversion.

376 are lowest over the period range from 10 s to 1000 s with slightly higher values for shorter and
 377 longer periods, likely because the coarse grid we use still does not allow the introduction of
 378 structures to fit the shortest periods, whereas long period data are typically more noisy (due
 379 to limited recording times) and difficult to fit. The misfit distribution over individual sites
 380 is relatively uniform in the central and northern parts but generally higher in the southern
 381 part. The southern part of the model is characterized by strong lateral resistivity variations
 382 in the VL and the conductive BF (see the surface panel in Fig. 10). Here, coarse model
 383 discretization and regularization prevented the introduction of stronger resistivity variations
 384 resulting in poorer fit, which we will improve at later stages. Static shift was largely corrected
 385 by the introduction of bow-tie shaped conductivity artefacts (see the surface panel in Fig.
 386 10) close to the sites. Data residuals (see Fig. 12b) exhibit a symmetric and zero-centered
 387 distribution, indicating no data-fit pathologies at this stage. The relatively large variance of
 388 the distribution will be reduced at later stages.

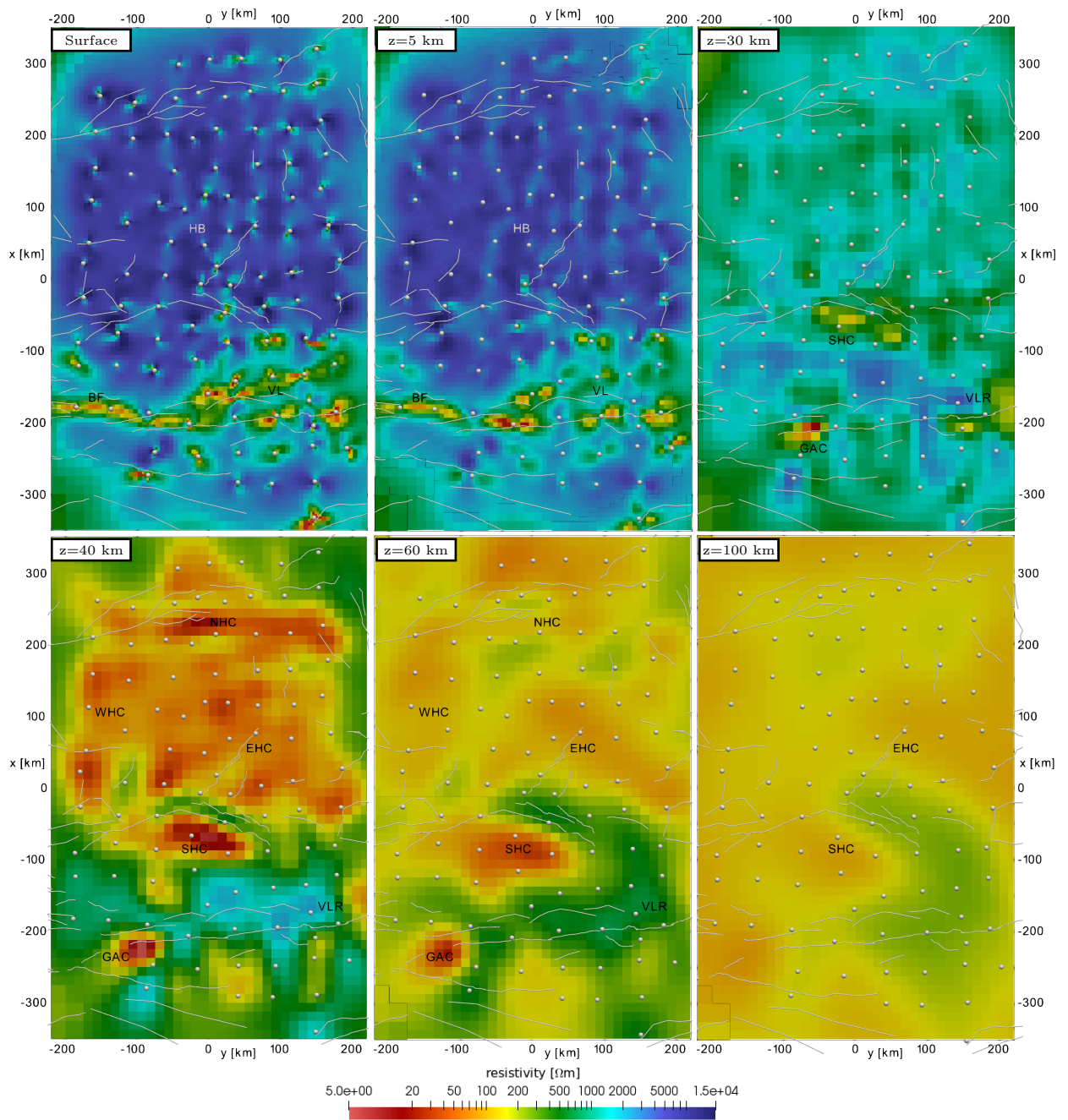


Figure 10. Horizontal slices through the best-fit model of inversion Stage II (model S2). Depth slices are shown at the surface and depths of $z = 5$ km, $z = 30$ km, $z = 40$ km, $z = 60$ km and $z = 100$ km (referred to sea level). Measurement sites are marked with grey spheres and major faults with grey lines. See Table 1 for abbreviations of model features, they include the resistive HB and the heterogeneously conductive VL with the BF in the upper crust. At a depth of 30 to 40 km the resistivity drops abruptly to form five distinct conductors in the lower crust and below, the SHC, NHC, WHC, EHC and GAC. Conversely, the VL is underlain by a resistor (VLR). With greater depths resistivity rises and at 100 km only the SHC and EHC remain discernible.

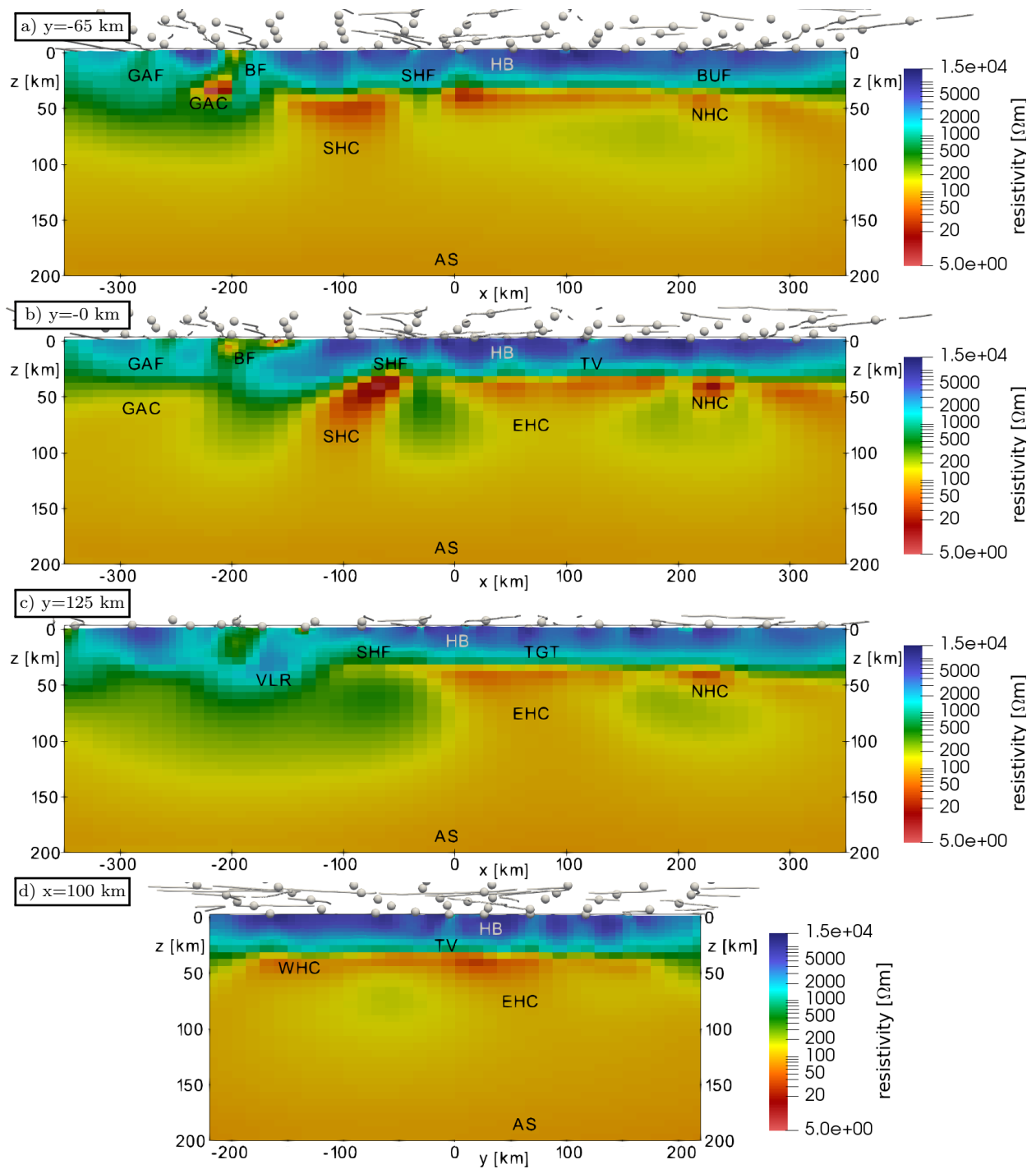


Figure 11. Vertical slices through the best-fit model of inversion Stage II (model S2). The slices are parallel to the x-axis at a) $y = -65$ km, b) $y = 0$ km, c) $y = 125$ km (approximately aligned with profiles 2, 4, and 6, see Fig. 1), and d) parallel to the y-axis at $x = 100$ km. Measurement sites are marked with grey spheres and major faults with grey lines. See Table 1 for abbreviations. The conductive BF can clearly be seen in the upper crust, whereas the GAF and SHF only show up as faint near-surface conductors. Additionally, it can be seen that the NHC is confined to a depth of 40 to 60 km (the lower-most crust), while the EHC and SHC extend downward to the AS. See also Fig. 10 for major model features.

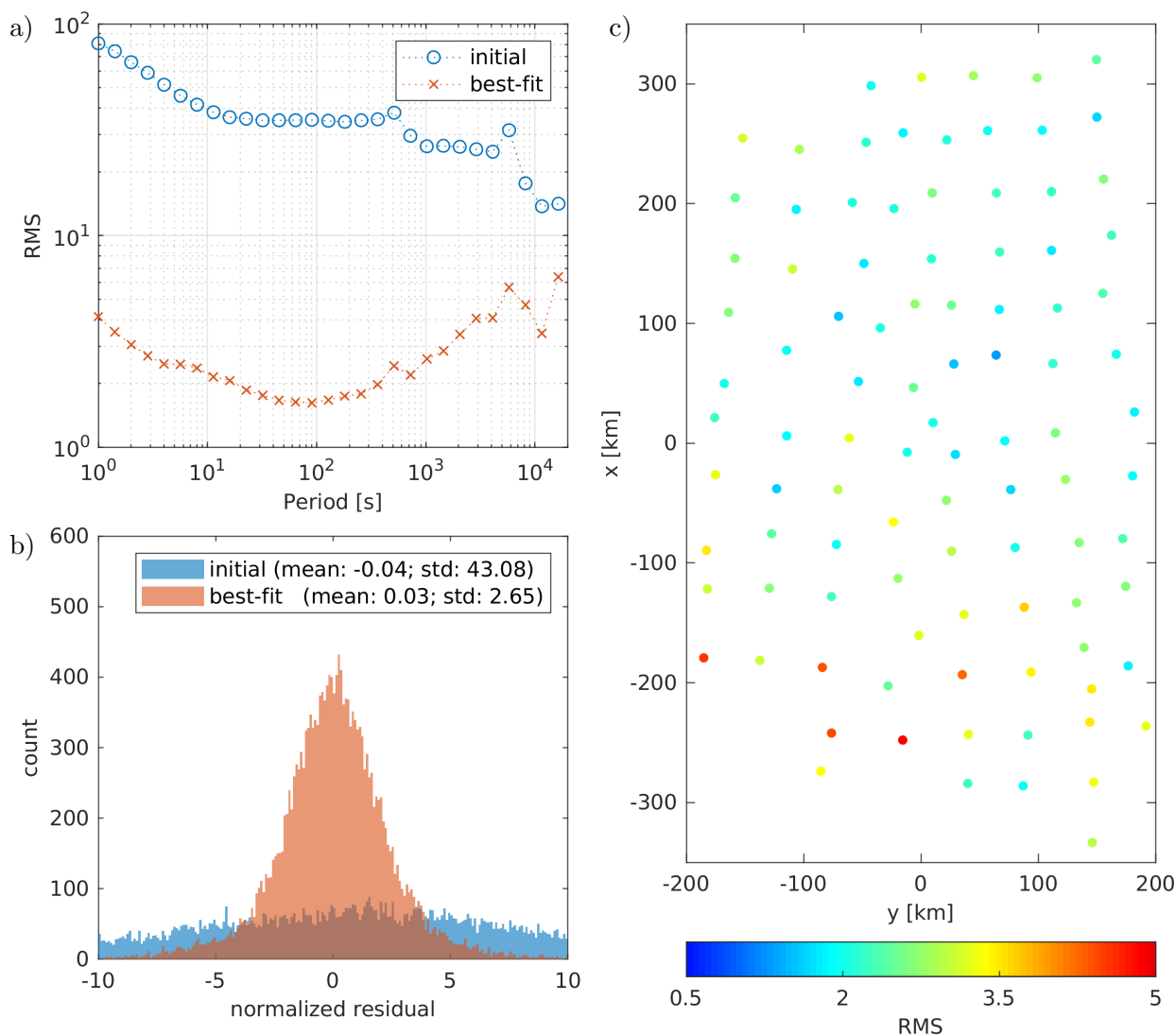


Figure 12. Data fit distribution of inversion Stage II. a) RMS value across periods for the initial and best-fit model; b) data residual histogram for the initial and best-fit model; c) RMS values at measurement sites for the best-fit model.

389 4.3 Stage III: 3-D inversion of all measurement sites

390 For the third stage, all measurement sites along profiles and near the TV and TGT were
 391 included (mostly telluric-only data). Adding the new data to the previous best fit 3-D model
 392 increased the RMS value to 33. After 12 iterations the inversion converged to a model with
 393 the RMS value of 2.1. Fig. 13 shows that an RMS value of 3 was reached after only four
 394 iterations, owing mostly to the compensated static shift effect. The best fit model (model
 395 S3) is shown in Figs. 14 and 15. In comparison to the results from the previous stage (Figs 10

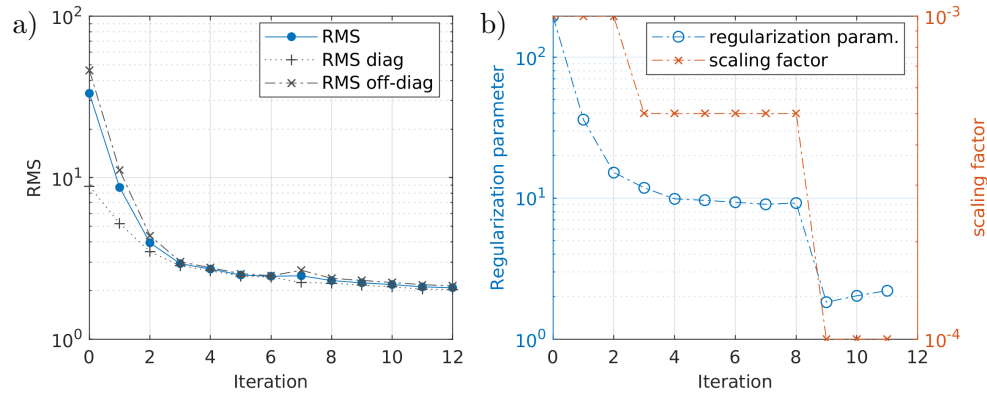


Figure 13. Progression of the RMS value (a) and regularization (see eq. 15) parameters (b) during Stage III of the inversion.

396 and 11), the large-scale structure remains the same, but resistivity contrasts became better
 397 resolved and some crustal structures appear more pronounced, such as the peculiar shape of
 398 the NHC. Additionally, the upper crustal resolution is improved (GAF, BF, and SHF) and
 399 new structures appear, for example the lowered resistivity in the upper crust below the TV
 400 and the TGT.

401 With an RMS value of 2.1, the data fit (Fig. 16) is overall better than in the previous
 402 stage, but with the same characteristics. Specifically, the misfit is slightly higher for short
 403 and long periods as well as for the southern sites. Additionally, there are three sites on profile
 404 P2 and two sites on profile P4 with a significantly higher misfit. These remaining problems
 405 are mainly due to the complex local 3-D structures and are resolved in the final stage of the
 406 inversion.

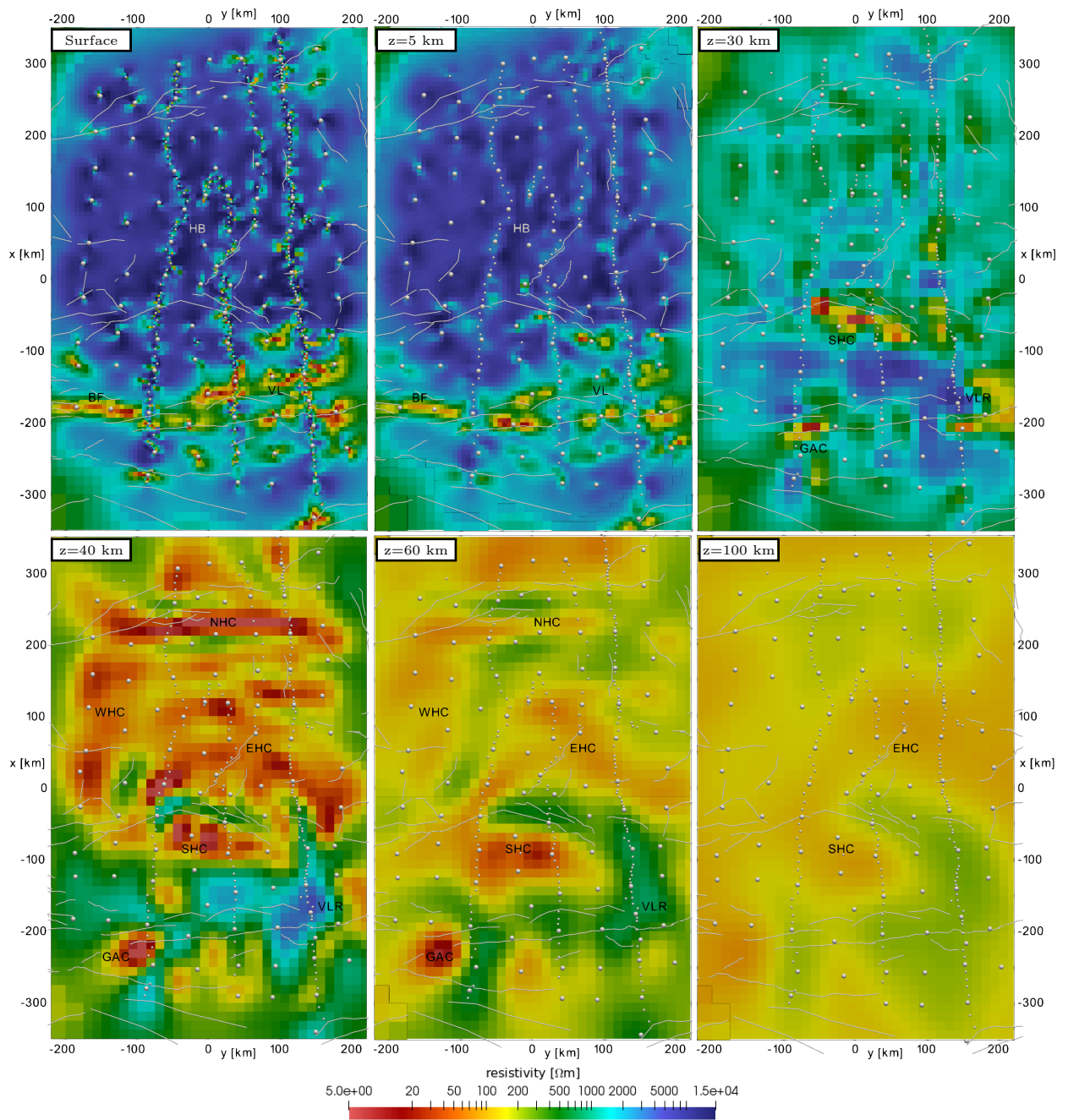


Figure 14. Horizontal slices through the best-fit model of inversion Stage III (model S3). Depth slices are shown at the surface and depths of $z = 5$ km, $z = 30$ km, $z = 40$ km, $z = 60$ km and $z = 100$ km (referred to sea level). Measurement sites are marked with grey spheres and major faults with grey lines. See Table 1 for abbreviations of model features. In comparison to the previous stage (see Fig. 10), model features are imaged more finely. The near surface along the profiles and the conductors in the lower crust ($z = 40$ km) especially benefit from the additional data included in this stage.

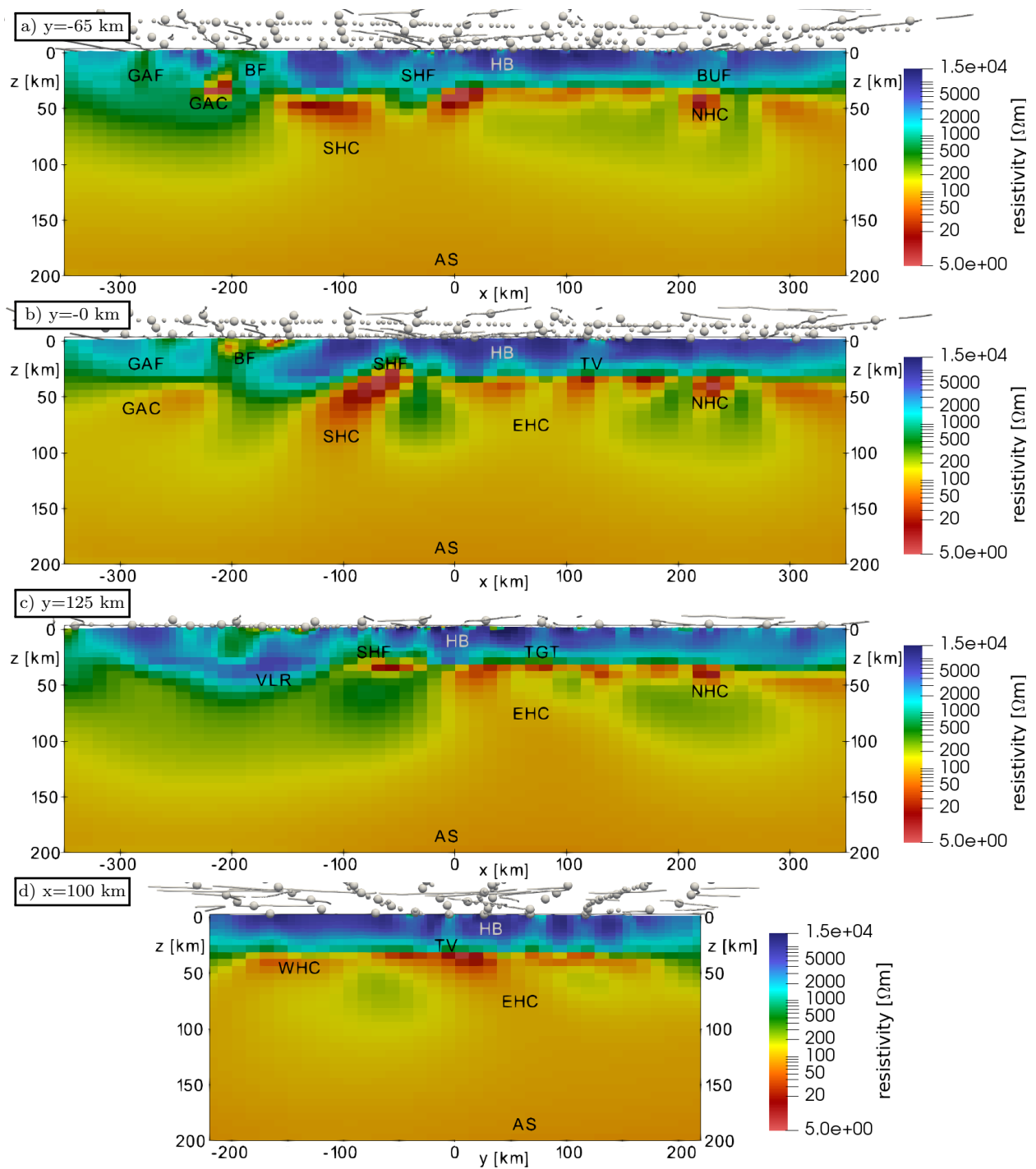


Figure 15. Vertical slices through the best-fit model of inversion Stage III (model S3). The slices are parallel to the x-axis at a) $y = -65$ km, b) $y = 0$ km, c) $y = 125$ km (approximately aligned with profiles 2, 4, and 6, see Fig. 1), and d) parallel to the y-axis at $x = 100$ km. Measurement sites are marked with grey spheres and major faults with grey lines. See Table 1 for abbreviations of model features. See Fig. 10 for major model features. In this model, conductive signatures can be seen in the upper crust below TV and TGT.

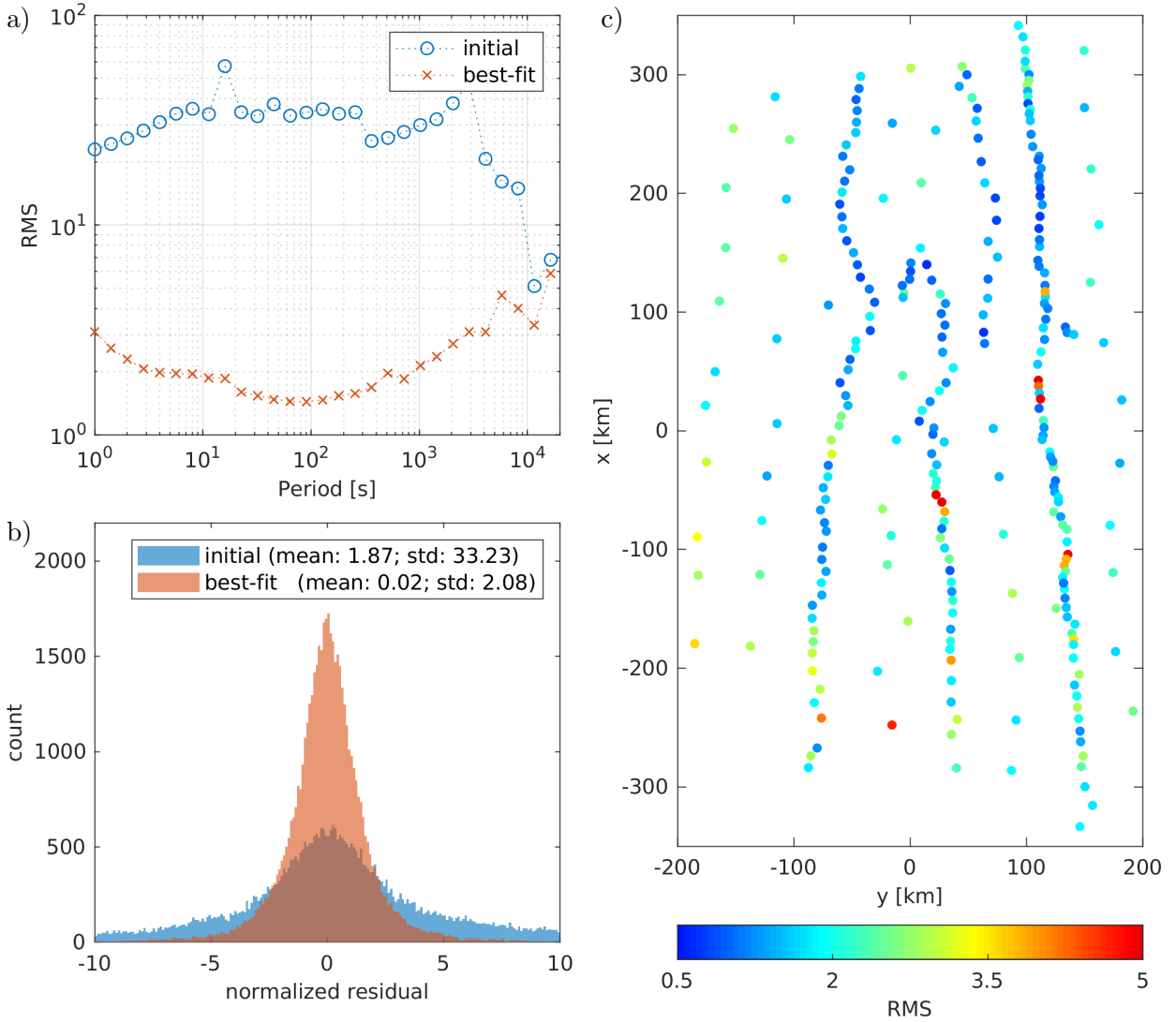


Figure 16. Data fit distribution of inversion Stage III. a) RMS value across periods for the initial and best-fit model; b) data residual histogram for the initial and best-fit model; c) RMS values at measurement sites for the best-fit model.

4.4 Stage IV: higher crustal resolution and short periods

For the last stage, short period data along the denser profiles were added and a finer mesh was used. As we will see, the mesh refinement around site locations and in the lower crust leads to a better fit for short period data.

Adding new data increases the RMS to a value of 8.9 when using the best fitting model from the previous stage. After 17 iterations a misfit of 1.86 was obtained (see Fig. 17). The obtained model (model S4) is shown in Figs 18 and 19. Compared to the previous stage,

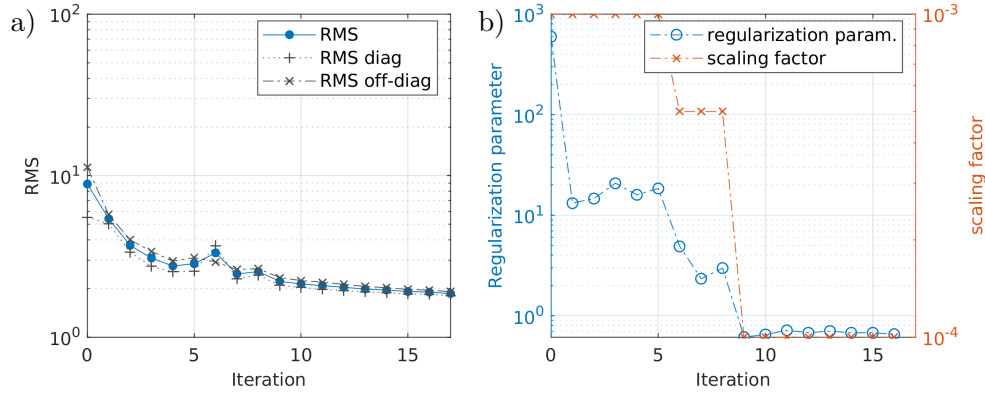


Figure 17. Progression of the RMS value (a) and regularization (see eq. 15) parameters (b) during Stage IV of the inversion.

414 the finer mesh leads to significantly improved resolution in the lower crust, which further
 415 enhanced the geometry and structure of the lower crustal conductors (NHC, EHC, SHC and
 416 WHC). By adding the short period data, the crust is imaged more finely and the resolution
 417 is close to that of the 2-D model by Comeau et al. (2018c).

418 The model fits the data well (Fig. 20). The overall higher misfit at longer periods ($>$
 419 1000 s, Fig. 20a) can be attributed to noisy long period data and the fact that the assigned
 420 error was likely too optimistic for these periods. Additionally, there are eight sites that
 421 have a RMS values > 3.5 , either due to noisy data and poor fit of the diagonal impedance
 422 components or because of unresolved local structures.

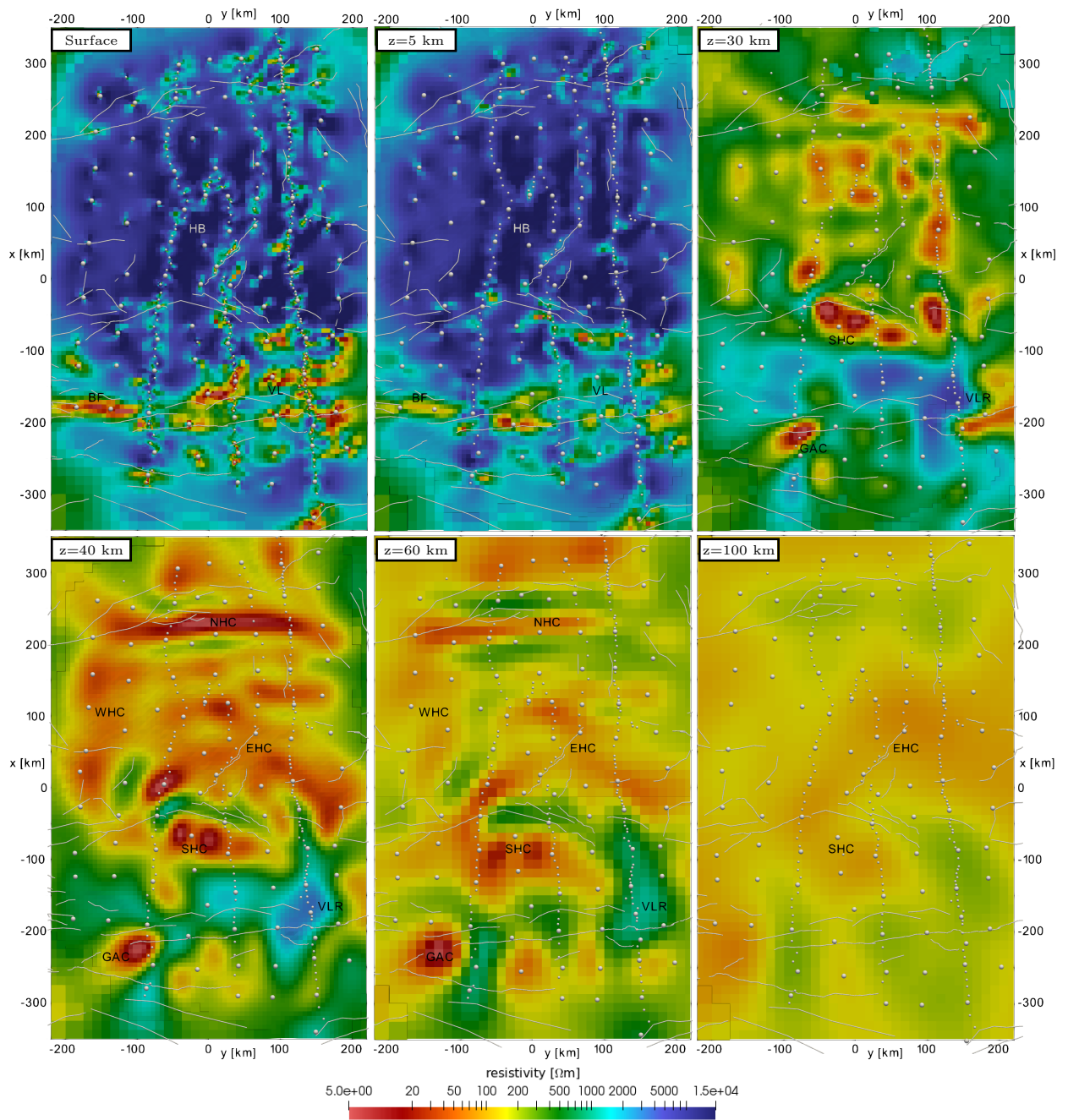


Figure 18. Horizontal slices through the final model of inversion Stage IV (model S4). Depth slices are shown at the surface and depths of $z = 5$ km, $z = 30$ km, $z = 40$ km, $z = 60$ km and $z = 100$ km (referred to sea level). Measurement sites are marked with grey spheres and major faults with grey lines. See Table 1 for abbreviations and Figs 10 and 14 for the model features.

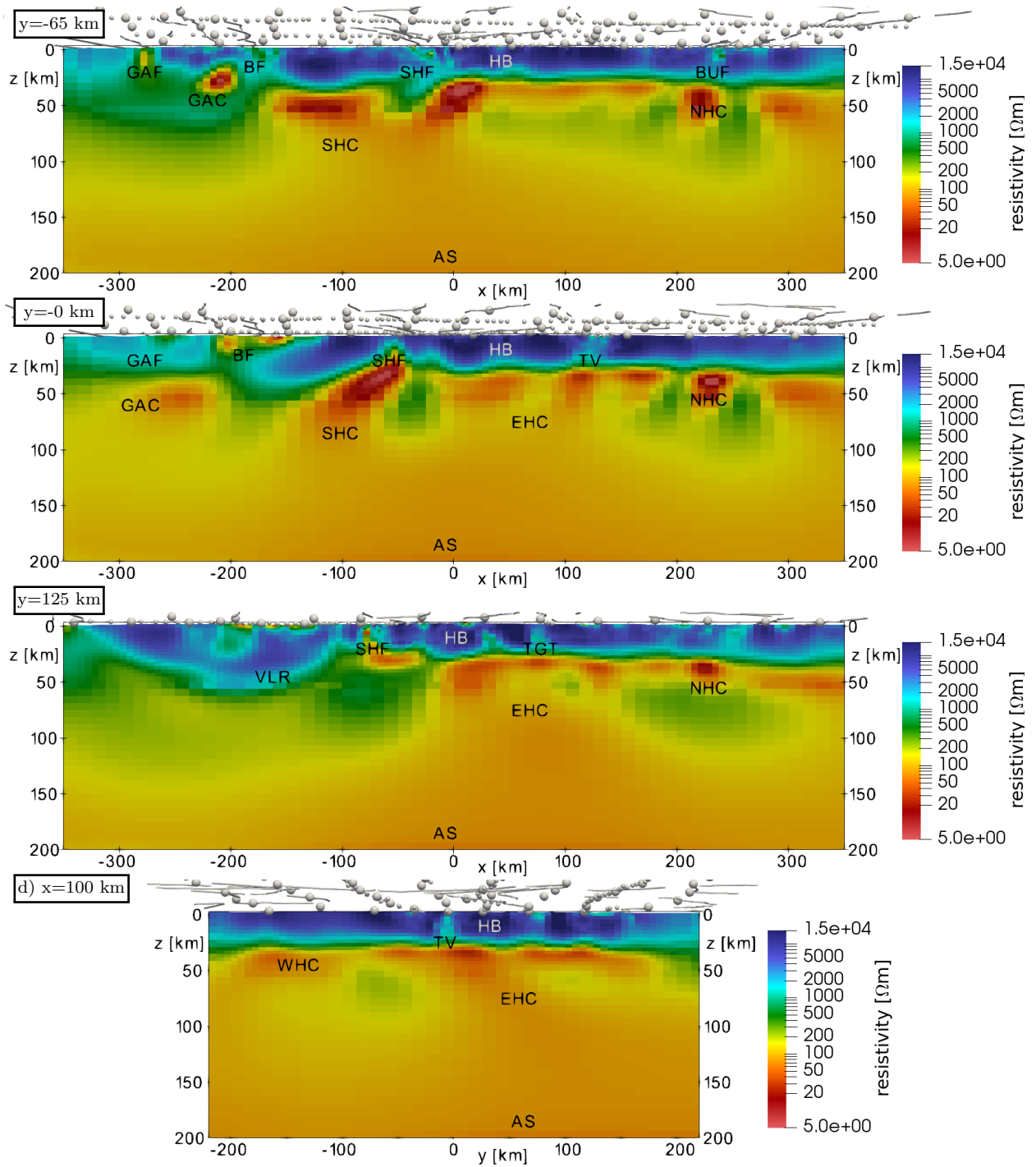


Figure 19. Vertical slices through the final model inversion Stage IV (model S4). The slices are parallel to the x-axis at a) $y = -65$ km, b) $y = 0$ km, c) $y = 125$ km (approximately aligned with profiles 2, 4, and 6, see Fig. 1), and d) parallel to the y-axis at $x = 100$ km. Measurement sites are marked with grey spheres and major faults with grey lines. See Table 1 for abbreviations and Figs 11 and 15 for model features. During this stage the BUF was resolved in some parts of the model.

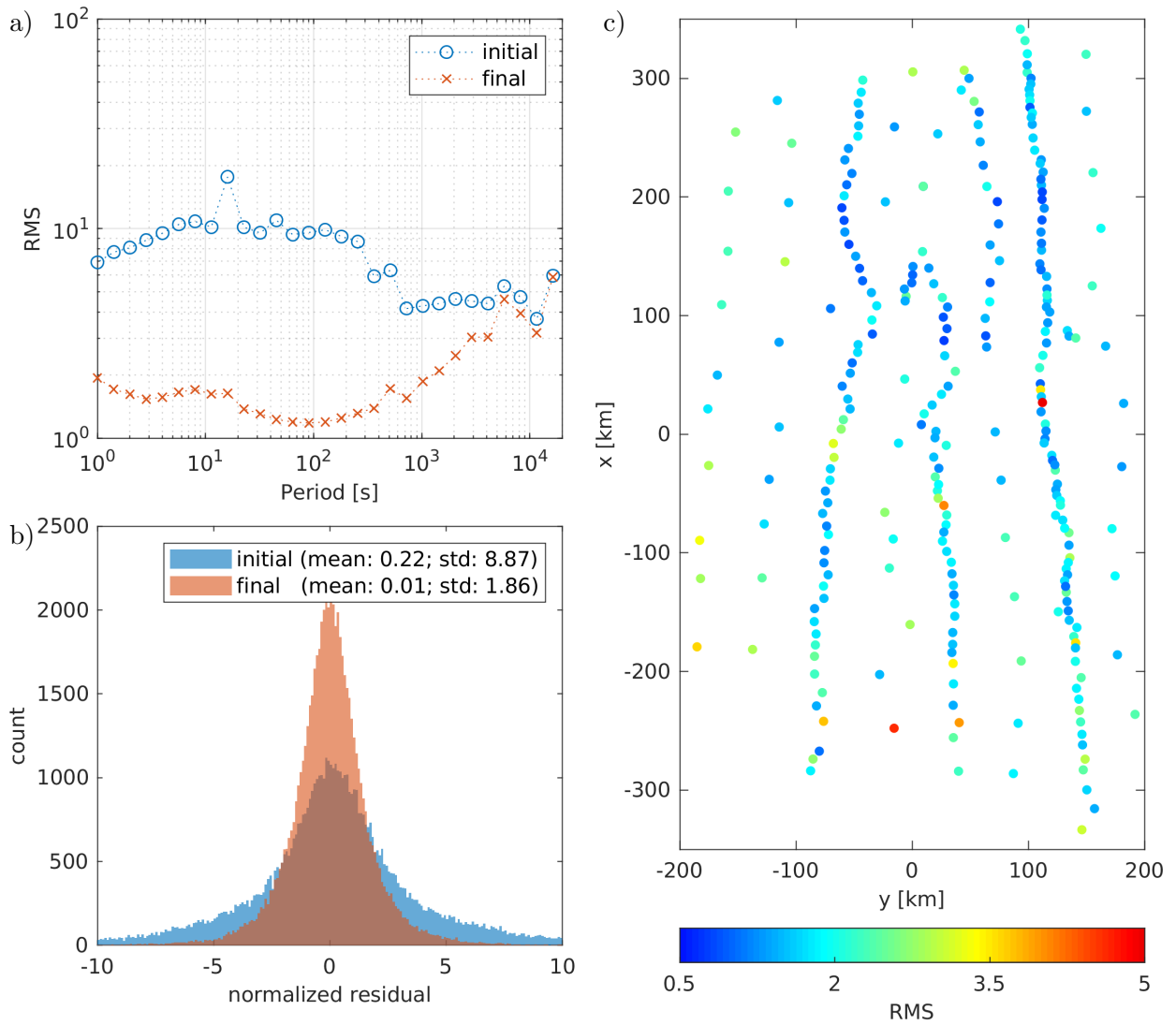


Figure 20. Data fit distribution of inversion Stage IV. a) RMS value across periods for the initial and final model; b) data residual histogram for the initial and final model; c) RMS values at measurement sites for the final model.

423

424 **5 DISCUSSION**425 **5.1 Inversion methodology**

426 In the previous section, we explained the four stage inversion strategy used to obtain
 427 the final resistivity model. Fig. 21 shows a comparison of the models S2, S3, and S4 for
 428 an exemplary area in the centre of the model. While larger features (HB, EHC, SHC, etc.)
 429 are already imaged in Stage II, the addition of profile sites during Stage III reveals smaller
 430 crustal features in more detail (SHF, TV, etc.) and gives a finer resolution for the structure
 431 of the EHC in model S3. Additional mesh refinement and the inclusion of short period
 432 data improves the results further, as is evident by the comparison of S3 and S4. The link
 433 between the SHC and SHF can be seen and TV becomes a prominent vertical conductor in
 434 the upper crust, located directly on top of a $40 \Omega\text{m}$ conductor at a depth of 35 km. Similar
 435 improvements from stage to stage can be observed for other features throughout the model
 436 (e.g. TGT, GAF, BUF, BF, CV)

437 During the first stage, a regionally averaged 1-D model was derived to be used as an
 438 initial model for the 3-D inversion. It is well known that the initial model can significantly
 439 influence the result of a 3-D inversion. To assess the influence of the 1-D model, we performed
 440 two inversion runs with identical settings to Stage II except for initial half-space models of
 441 $500 \Omega\text{m}$ (Model S2HS500) and $1000 \Omega\text{m}$ (Model S2HS1000), see the supplementary material
 442 Sec. S3.1 and S3.2. After 18 iterations S2HS500 achieved a RMS value of 3.1 and S2HS1000
 443 achieved a RMS value of 3.2 after 19 iterations. Both are significantly higher than the RMS
 444 value of 2.65 achieved after Stage II with a 1-D starting model (Sec. 4.2).

445 The recovered conductivity structure is similar to S2 only down to a depth of about 70 to
 446 100 km. Below that depth no new features were introduced. Furthermore, it can be seen that
 447 the arbitrary choice of the initial half-space resistivity influences the overall resistivity of the
 448 final model, the average resistivity of S2HS500 is lower than that of S2HS1000. Although the
 449 initial 1-D model from Stage I has an influence on the results of Stage II, there is no arbitrary

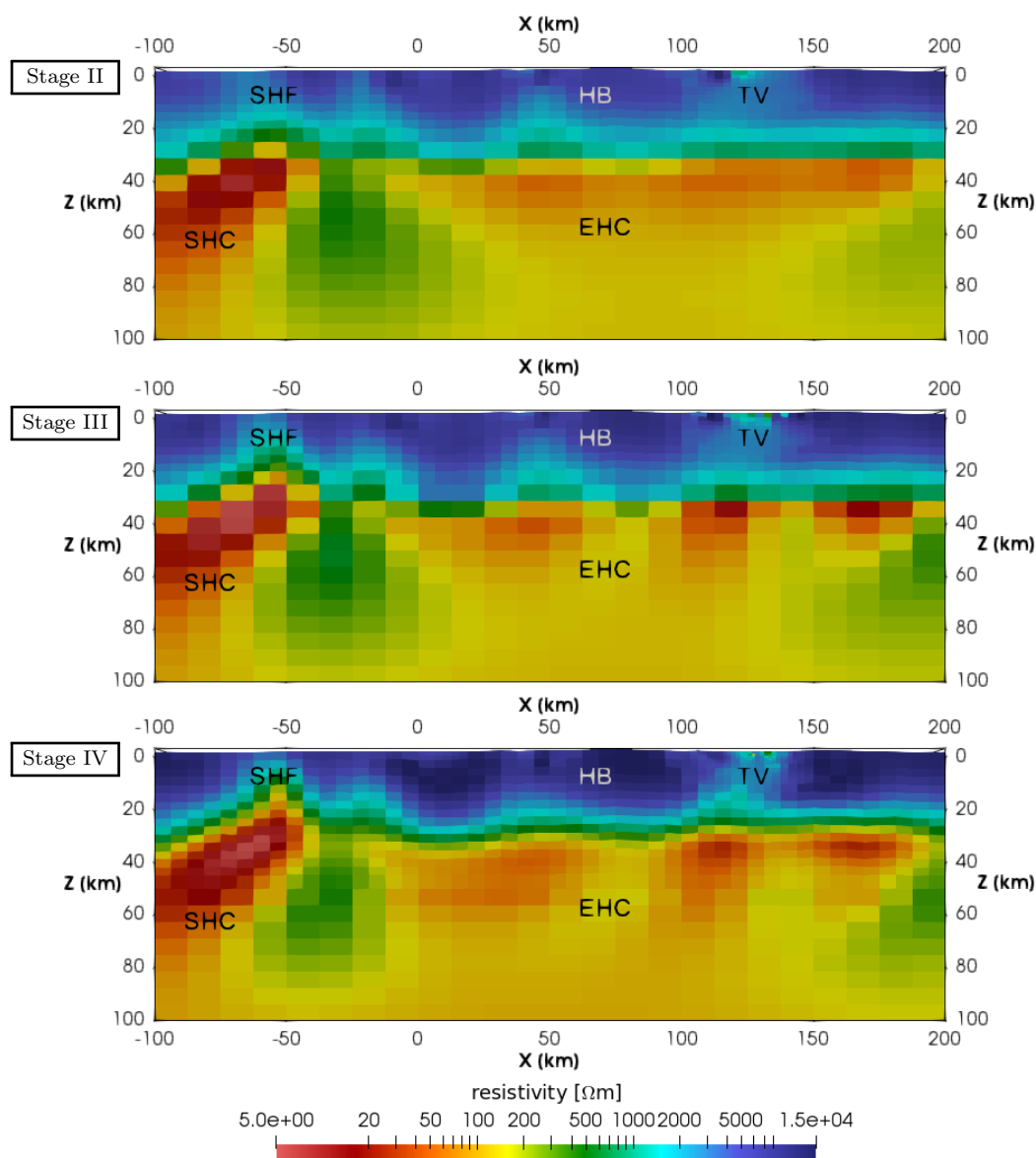


Figure 21. Comparison of the three stages of the 3-D inversion on a vertical slice in x -direction at $y = 0$. See Table 1 for abbreviations and Figs 11, 15, and 19 for major model features.

450 choice of resistivity values. Instead, the initial model is defined by the regionally averaged
 451 impedances and represents the best-fitting 1-D model, with the caveat that measurement
 452 sites south of the SHF were discarded (due to the lack of a consistent regional 1-D structure,
 453 as outlined in the Sections 4.1 and 2.3). The regional 1-D model north of the SHF is thereby
 454 imposed on the region in the south. However, this proves to be not a problem because the
 455 1-D model enters Stage II only as an initial model, not as a reference for the regularization.
 456 The strong conductivity contrast at $z = 25$ km (see Fig. 8) is almost completely removed

457 and a laterally more heterogeneous resistivity structure is introduced for the VL and the
 458 region south of the SHF to fit the data there.

459 Separate inversion Stages II and III were necessary to ensure that the regional resistivity
 460 structure was recovered first, before smaller and shallow structures were fitted. If the Stages
 461 II and III are combined (see Model S2+3 in the supplementary material S3.3) the inversion
 462 is strongly biased to the eastern part of the grid (between P2 and P6, see Fig. 1) due to the
 463 higher number of stations there. This leads to the western part of S2+3 (west of P6) being
 464 fitted only in the end of the inversion process (starting at iteration 15 of 23), resulting in
 465 a significantly higher RMS value for sites along line 8, in comparison with the entire grid.
 466 The recovered model happens to be virtually identical to model S3. However, because of the
 467 bias to the eastern sites for most of the iteration steps, a separated approach is preferred,
 468 whereby the regional 3-D structure is recovered from the grid stations first, and afterwards
 469 smaller structures are revealed due to the additional data from the profiles introduced during
 470 Stage III.

471 For the same reason, short period data (0.09 s to 1 s) with penetration depths as small
 472 as 2 km were added in Stage IV, the final stage of the inversion process. The short period
 473 data were accompanied by a mesh refinement, which increased the computational cost of
 474 a single iteration by a factor of 2.4. By fitting the regional structure on the coarser mesh
 475 first and using the fine mesh only in the end, the computational cost for the entire inversion
 476 process was significantly reduced.

477

478 5.2 Geologic interpretation

479 5.2.1 Upper mantle structure

480 Broad array coverage and the inclusion of long-period measurements enable sensing con-
 481 ductivities down to ≈ 200 km. The 3-D model reveals significant low-resistivity (30–100 Ωm)
 482 features (SHC and EHC) below the Hangai Dome at depths greater than approximately
 483 70 km, consistent with the previous 2-D model (Comeau et al. 2018c). Calculations confirm

484 that olivine in the upper mantle containing water up to the solubility limit is inadequate
485 to explain the conductivity observed (Yoshino et al. 2009; Comeau et al. 2018c). Therefore,
486 this feature is interpreted as an upwelling asthenosphere that contains partial melt, and it
487 is likely a zone of melt generation. To the south, in the South Gobi region, the LAB depth
488 appears to increase significantly, again consistent with the 2-D model of Comeau et al.
489 (2018c). The geometry of the LAB is consistent with previous seismic profile measurements
490 that indicate an irregular dome-shaped LAB below central Mongolia (Petit et al. 2008).
491 In accord with this interpretation, Bouguer gravity models revealed a localized low-density
492 structure at a depth of 80 – 125 km below the central Hangai (Tiberi et al. 2008, see Fig. 1).
493 Furthermore, analysis of erupted mantle xenoliths from central Mongolia suggests long-lived
494 (< 30 Ma) and shallow (< 70 km) melting from an asthenospheric source (Ionov 2002; Barry
495 et al. 2003; Hunt et al. 2012).

496 What is unique about the 3-D model presented here is that, for the first time, the non-
497 uniformness of the asthenospheric upwelling and its lateral complexities are imaged. Two
498 main peculiarities emerge from the recovered shape of the upwelling. Firstly, one arm is
499 imaged below the eastern Hangai Dome, labelled EHC in Fig. 22. It is centred below the
500 eastern part of the dome and dips eastward where it appears rooted at depths greater than
501 150 km. In fact, this anomaly aligns very closely with the location of many cenozoic vol-
502 canic provinces (Ancuta et al. 2018, see Fig. 1), elevated heat-flow measurements (Ionov
503 2002, and references therein, see Fig. 1), indicative of advective heat transfer, and the high-
504 est concentration of present-day hydrothermal activity in the form of meteoric hot springs
505 (Oyuntsetseg et al. 2015; Ganbat & Demberel 2010, see Fig. 1).

506 It is remarkable that these features, together with the upwelling asthenosphere, are con-
507 fined to the eastern part of the Hangai Dome. In contrast, there are little known signs of
508 volcanism and geothermal activity in the western part of the Hangai Dome, despite its topo-
509 graphic similarity to the eastern part. Intriguingly, seismic models identified a deep-rooted
510 seismic low-velocity zone further to the east that is reaching upwards below the eastern

511 Hangai and the Hentey plateau (Zhang et al. 2017; Chen et al. 2015) that may represent an
512 extension of the low-resistivity feature observed here.

513 Secondly, a smaller arm of the upwelling asthenosphere is imaged south-west of the
514 Hangai Dome, labelled SHC and depicted in Fig. 23. This is particularly intriguing because
515 it is not below the Hangai Dome itself, but rather south of the dome and the SHF zone.
516 It is, however, below a topographic high. Both arms of the upwelling are connected with a
517 continuous conductive region below 150 km. The origin of such an asthenospheric upwelling
518 remains unexplained. However, it is very likely responsible for the intraplate volcanism
519 observed across the Hangai Dome. In addition it may be responsible for lowering the lower-
520 crustal viscosity by increasing the temperature at the base of the crust.

521 However, it is unknown what relation the smaller secondary arm of the upwelling has to
522 the main arm below the eastern Hangai. Other open questions are whether there exist other
523 arms of the upwelling, for example below the Hovsgol rift region north of the Bulnay fault,
524 and if the volcanism of that region is connected at depth to the same Hangai upwelling.

525

526 5.2.2 Implications for geodynamic models

527 The origin of the asthenospheric upwelling remains purely speculative at this time. His-
528 torically, explanations for intracontinental uplift have been dominated by arguments for
529 hot, mantle-rooted plumes (e.g. Windley & Allen 1993). However, modern geophysical and
530 petrological evidence is often not consistent with this explanation (e.g. Barry et al. 2003). In
531 central Mongolia, inconsistencies include a lack of low seismic velocities at greater depths,
532 a lack of concentrated high heat flow, low volumes of volcanism, and a lack of spatial or
533 temporal volcanic pattern (e.g. Barry et al. 2003). The moderate resistivity values observed
534 in this study imply low-percent partial melts generated in the mantle due to decompression
535 melting and hence suggest a low-heat flux, small-scale asthenospheric upwelling.

536 From seismic studies, it is known that the lithosphere is thick below the Siberian Cra-
537 ton (up to 225 km), which requires a large lithospheric step (up to 150 km) between the
538 Siberian craton and the Hangai Dome, where the lithosphere is thin (> 70 km). This leads

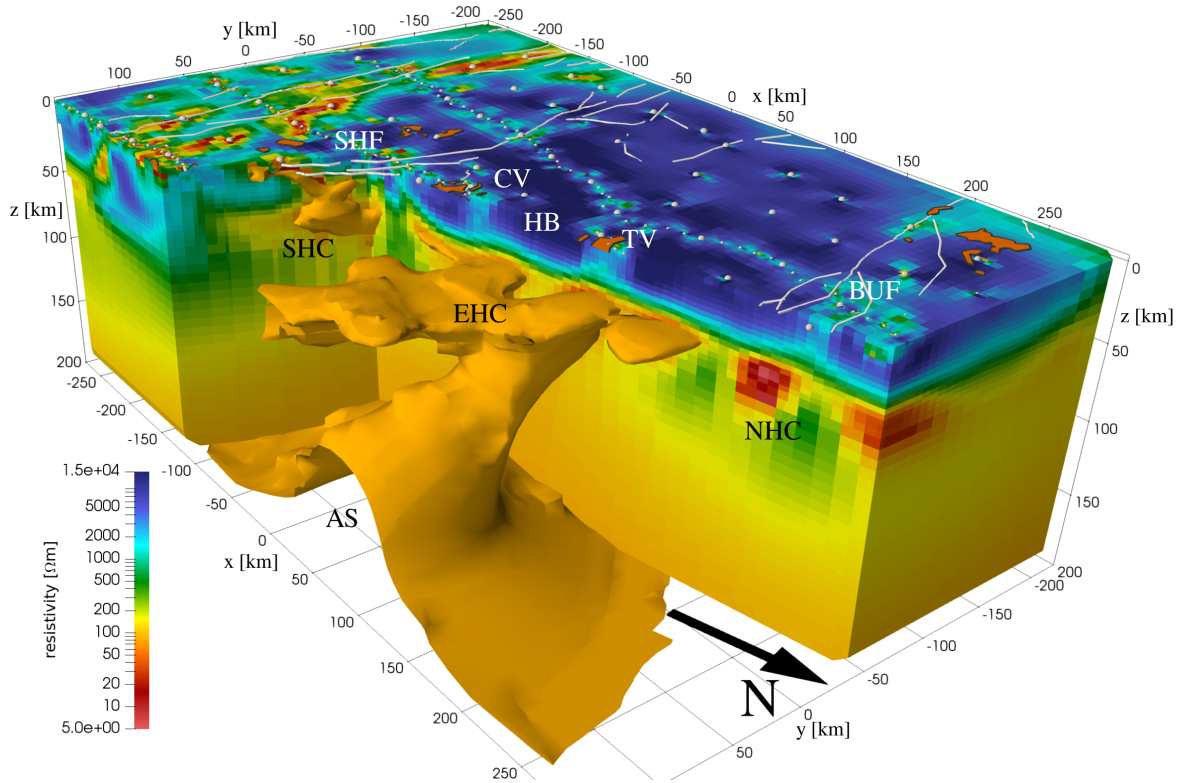


Figure 22. 3-D cutaway view of the model S4. The EHC and the eastern arm of the asthenospheric upwelling are shown with a $85 \Omega\text{m}$ isosurface. White spheres indicate measurement sites, white lines are faults, and volcanic provinces are orange.

539 to speculation that edge-driven convection could cause thermal erosion of the lithosphere
 540 (e.g. Bao et al. 2014).

541 Alternatively, there is good evidence that a delamination event could fit the observa-
 542 tional constraints. Previous studies demonstrated that removal or thinning of the sub-crustal
 543 lithosphere by a delamination process, whereby the dense sub-crustal lithosphere decouples
 544 and peels away from the crust, foundering and sinking into the asthenosphere, results in a
 545 small-scale upwelling of the buoyant asthenosphere (e.g. Meissner & Mooney 1998; Kay &
 546 Kay 1993; Bird 1979). Critically, numerical modelling studies revealed that a weak lower-
 547 most crust, as observed in central Mongolia, is required to trigger a delamination event
 548 (Krystopowicz & Currie 2013).

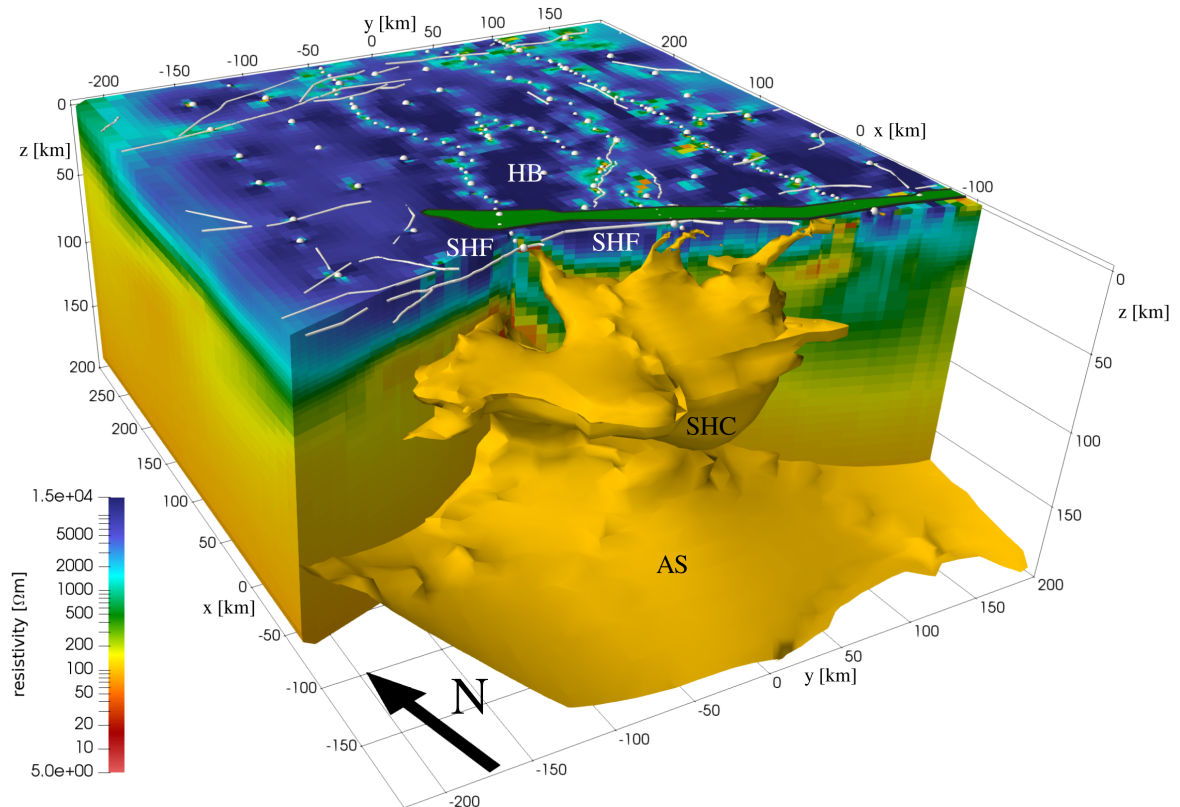


Figure 23. 3-D cutaway view of the model S4. The SHC and the southern arm of the asthenospheric upwelling are shown with a $100 \Omega\text{m}$ isosurface. White spheres indicate measurement sites, white lines are faults, and the green area is the Bayankhongor Ophiolite Belt (Buchan et al. 2001).

5.2.3 Lower crustal structure

One of the most prominent and best resolved features revealed by the 3-D resistivity model is the unexpected heterogeneous low-resistivity ($10\text{--}100 \Omega\text{m}$) zone imaged in the lower crust ($30\text{--}50 \text{ km}$; labelled EHC, SHC, WHC, NHC). This feature is pervasive throughout the central Hangai but ends abruptly at the South Hangai fault zone. In the northern Hangai region, near the Bulnay fault, this low-resistivity zone is organized into several east-west trending cylinders (with NHC being the most prominent one, see Fig. 18), which is a robust modelling result. The cylinder-like structures have a width of approximately 20 km , and are roughly parallel to the Bolnay fault zone and aligned with GPS measurements that indicate an eastward-motion of the Hangai block (Calais et al. 2003).

Because geochemical evidence is inconsistent with long-lived crustal melt storage below

561 the Hangai Dome (e.g. Harris et al. 2010), the preferred explanation for these low-resistivity
562 zones are fluids. Highly saline fluids can be exsolved by metasomatism in dehydration and
563 devolatilisation reactions (Manning 2018). Connolly & Podladchikov (2004) predicted that
564 in compressive tectonic settings an inverted stress gradient beneath the brittle-ductile tran-
565 sition causes fluids to become trapped in the lower crust. Furthermore, numerical hydrome-
566 chanical models can explain how spatial focusing of the fluid source flux can create hydraulically
567 connected fluid-rich domains within the ductile crust (Connolly & Podladchikov 2013).
568 This conceptual model is remarkably consistent with the MT evidence for lower crustal fluid-
569 rich domains in central Mongolia. In addition, the pattern of fluid focusing is expected to
570 be superimposed on large-scale tectonic deformation patterns, such as compression and ex-
571 trusion. Therefore, in central Mongolia, such fluid-domains should form extended cylinders,
572 compatible with what is observed.

573 This fluid content substantially changes the rheology and significantly reduces the crustal
574 strength and viscosity (e.g. Liu & Hasterok 2016). This is consistent with evidence from post-
575 seismic slip measurements that also indicate a significantly reduced viscosity in the lower
576 crust of Mongolia, of several orders of magnitude, as compared to the upper crust (Vergnolle
577 et al. 2003). Further evidence for a weak lower crust is given by the depth distribution of
578 local seismicity, no earthquakes are observed deeper than approx. 20 – 25 km (Meltzer et al.
579 2019). A weak lower crust must be considered in future geodynamic and mechanical models
580 of the tectonics in this region. It is an open question how these fluid-rich domains change
581 northwards across the Bolnay fault zone and eastwards outside the Hangai block.

582

583 *5.2.4 Upper crustal structure*

584 **5.2.4.1 Fault zones** In general, the upper crust below the Hangai Dome is very resis-
585 tive (2000 – 40000 Ωm , labelled HB). This can be explained by a pre-Cambrian, cratonic
586 basement (Cunningham 2001). In the VL, the near-surface layer (< 0.5 km) has a highly
587 variable resistivity (10 – 2000 Ωm) caused by porous sediments (Ganbat & Demberel 2010).
588 Elsewhere, some of the anomalous upper crustal features are attributed to fault zones. They

589 are regions of fractured, weakened crust that often have circulating fluids that act to in-
 590 crease their conductivity, therefore they are commonly imaged as strong crustal conductors
 591 (Unsworth & Bedrosian 2004).

592 South of the Hangai Dome lies the SHF system (Walker et al. 2007; Cunningham 2001),
 593 which marks an important terrane boundary (Badarch et al. 2002) and an ancient suture
 594 zone created during the closure of the Mongol-Okhotsk ocean (Van der Voo et al. 2015). In
 595 the resistivity model the fault zone is imaged as a strong crustal conductor, connected with
 596 the SHC and the southern arm of the upwelling (see Fig. 23). However, in contrast to previous
 597 2-D results from Comeau et al. (2018c), the conductive feature is not detected continuously
 598 along the expected fault trace, instead several disconnected fragments are imaged in the
 599 upper crust (Fig. 23). Narrow (< 5 km), tendril like anomalies extend upwards from the
 600 SHC in the lower crust to the surface. This may be associated with its mineral potential
 601 (discussed below) or that some parts of the fault have been recently reactivated (Walker
 602 et al. 2007).

603 Remarkably, the lower crustal conductive zone (discussed above) terminates abruptly
 604 at this fault zone. Hence any lower crustal fluids are confined below the Hangai Dome,
 605 indicating the importance of this fault zone as a major crustal boundary.

606 Along the northern BUF zone, the resistivity model shows that at near surface depths
 607 (< 2 km) conductive anomalies ($50 - 1000 \Omega\text{m}$) appear coincident with the surface trace
 608 of the fault zone in Fig. 22. These can be attributed to a crush zone and to circulating
 609 meteoric fluids. However, at depth the fault is not imaged as a strong conductor. Perhaps
 610 an electrical signature is absent because the fault is dry and locked, as expected for fault
 611 zones with large and infrequent ruptures (Unsworth & Bedrosian 2004; Rizza et al. 2015).
 612 Furthermore, it appears the fault zone is independent of the lower crustal fluid zones (no
 613 drainage), indicating that the lower reaches of the fault are sealed.

614 The BF zone that runs along the (transpressional) Gobi-Altai mountain range, and which
 615 ruptured with a moment magnitude of 8.1 in 1957 (Rizza et al. 2015), is suspected to be
 616 lithospheric-scale (Badarch et al. 2002; Calais et al. 2003). Furthermore, this fault zone rep-

resents a significant terrane boundary (Badarch et al. 2002). Contrasting crustal properties observed across this zone reflect the rheological differences between accreted terranes of different origins (see Guy et al., 2015 and references therein; Comeau et al., 2019). Anomalous conductive features ($30 - 100 \Omega\text{m}$) are observed along the GAF system. These dominate the shallow structure and are interpreted to mark terrane boundaries.

5.2.4.2 South Hangai mineralized zones Immediately south of the SHF is an obducted ophiolite belt, the Bayankhongor Ophiolite Belt (green area in Fig. 23), which is possibly the longest continuous ophiolite belt in the world (Buchan et al. 2001). This region hosts the Bayankhongor Metallogenic Belt, an economically significant ore zone, including important sources of gold and copper.

Anomalous, strongly conductive features ($20 - 40 \Omega\text{m}$) stretch from the mid-crust to the surface on the the southern edge of the Bayankhongor Ophiolite Belt (see Fig. 23). Mineralization zones commonly have conductive signatures from associated sulphide mineralogy and metamorphic processes and these are likely imaged in the resistivity model.

5.2.4.3 Tariat and Chuluut volcanic zones The Hangai Dome contains dispersed, low-volume, intraplate, alkaline basaltic volcanism (average of 50% silica and 4% sodium) (e.g. Ancuta et al. 2018; Hunt et al. 2012; Barry et al. 2003, see Fig. 1 for the volcanic provinces in the Hangai). The Tariat region, the youngest volcanic zone in the Hangai with eruptions as recently as 5000 years ago, contains numerous volcanic cones (approx. 1000 m wide and 100 m high) with volcanic fields from the Holocene (< 11000 years) (Barry et al. 2003). The Chuluut region (100 km to the south) is the largest volcanic field in the Hangai. Lavas erupted here, are dated from 6 to 0.3 M years (Ancuta et al. 2018).

The MT data are used to generate high-resolution electrical resistivity models in these regions and can give insights into the structure of this region. Anomalous, conductive ($400 - 1500 \Omega\text{m}$) features in the upper crust can be seen in Fig. 22 below the volcanic zones of Tariat and Chuluut (TV and CV respectively, along P4). These conductive vertical features in the upper crust may represent hydrothermal alteration from ancient and transient conduits of

644 hot magma as it moved through the crust by dyking or along pre-existing local crustal
 645 weaknesses such as re-activated faults (e.g. Cashman & Sparks 2013), which would produce
 646 a small but detectable electrical signature (Comeau 2015; Comeau et al. 2016). No crustal
 647 magma storage is expected, due to evidence for fast magma ascent directly from a single
 648 parent source at mantle depths from petrological analysis (Harris et al. 2010; Hunt et al.
 649 2012). These anomalous features are spatially associated with the surface expressions of
 650 volcanism (volcanic cones and calderas) and modern-day hydrothermal activity (hot springs).

651 Below these volcanic regions, the upper mantle shows an upwelling asthenosphere (see
 652 Sec. 4.4), indicating the source region where melt for the intraplate volcanism is generated
 653 (> 80 km). This interpretation supported by petrological analysis of basaltic lavas that
 654 indicate long-term partial melting from a single mantle source (70 – 100 km). Therefore,
 655 the Tariat and Chuluut volcanism can be traced throughout the lithospheric column, from
 656 the melt source at the top of the upwelling asthenosphere to the hydrothermal alteration
 657 signature of ancient magma conduits in the upper crust. This is, therefore, a nice test of our
 658 inversion strategy that was designed to bridge multiple scales.

659 **6 CONCLUSIONS**

660 In this study we present the first 3-D resistivity model of the Hangai and Gobi-Altai region in
 661 Mongolia. The presented model successfully resolves features across multiple spatial scales,
 662 featuring small (< 5 km) crustal resistivity structures along with large-scale regional resis-
 663 tivity variations (extending more than 100 km) at the Lithosphere-Asthenosphere boundary
 664 within the same self-consistent model.

665 Magnetotelluric data were acquired over an area of 650×400 km² in the Hangai and
 666 Gobi-Altai mountains in central Mongolia. The project aimed at studying both regional
 667 lithospheric setting and the corresponding interactions with shallow crustal features, in-
 668 cluding local volcanism, geothermal activity and faulting. Therefore, we designed a station
 669 layout that combines a regularly spaced 50 km grid with denser spacing along profiles and
 670 in local areas of interest that have a spacing as small as 3 to 5 km. Efficient data acquisition

671 was achieved by the use of telluric-only instruments and deriving telluric-magnetotelluric
672 transfer functions for the profiles.

673 The technical aspects were addressed by using a finite-element method (FEM) inversion
674 algorithm based on non-conforming hexahedral meshes, which facilitates multi-scale model
675 parametrizations and allowed the incorporation of local topography while keeping computa-
676 tional cost feasible. We further developed a multi-stage inversion methodology, whereby we
677 gradually image various scales by including more sites and using a wider period range. For
678 Stage I, a regional 1-D resistivity model was derived to act as an initial model for the 3-D
679 inversion in Stage II, which included data from the grid sites. The resulting model was then
680 passed on to Stage III, where all sites with denser spacing were added, followed by Stage
681 IV with an extended period range and a finer mesh. This approach decreased the risk of
682 landing in a geologically implausible local minimum of the parameter space. As a result, we
683 obtained a resistivity model that accurately resolves small resistivity structures in the crust
684 together with regional resistivity variations down to the asthenosphere.

685 This approach can further be extended to both larger and smaller scales. The use of
686 long period instruments on a coarser grid could extend the model resolution beyond the
687 lithosphere-asthenosphere-boundary. A focused inversion, limited to a small subset of the
688 region but using a finer grid and short period transfer functions, could act as a high resolution
689 fifth stage and facilitate local studies of mineralized (Comeau et al. 2018b) and geothermal
690 zones (Batmagnai et al. 2019).

691 The final model images a prominent low-resistivity zone in the upper mantle, which is
692 attributed to partial melting within an asthenospheric upwelling. It reveals the complex
693 geometry of the upwelling, which appears rooted below the Eastern Hangai Dome with a
694 second smaller upwelling southwest of the Hangai Dome.

695 Thanks to the resolution across multiple spatial scales, surface observables (such as faults,
696 volcanic provinces and geothermal areas) can be linked with resistivity structures from the
697 shallow upper crust, down to the lithosphere and even asthenosphere. Among them are
698 the locations of the young Tariat and Chuluut volcanic zones, which are associated with

699 conductive features that can be traced throughout the crust and lithosphere, attributed
700 to past magma ascent and eruption events that have left their electrical signatures due
701 to hydrothermal alteration. Furthermore, the Gobi-Altai and South Hangai fault systems
702 are conductive features that dominate the shallow structures and, in the case of the South
703 Hangai fault system, some surficial conductors are coincident with well known mineralized
704 zones. Interestingly, these conductive anomalies can be traced uninterruptedly downward to
705 the second smaller upwelling southwest of the Hangai Dome.

706 The crustal structure is dominated by a terrane boundary along the South Hangai Fault
707 System, separating the southern marine terrane of the Gobi Altai from the cratonic Hangai
708 Block. While the upper crust of the Hangai Block is generally found to be highly resistive,
709 the lower crust consists of well-resolved low-resistivity zones in cylinder-like shapes. The
710 strong drop in resistivity at a depth of 30 – 35 km is interpreted as the transition to the
711 ductile lower crust, in good agreement with the depth distribution of the local seismicity.

712 The structural information from the resistivity model and their geologic implications
713 will provide crucial information to constrain the formation of the Hangai Mountains and
714 gain insight in intracontinental deformation and intraplate volcanism. The model presented
715 here, is generally consistent with a delamination process as the cause for volcanism and
716 uplift, however, more information is required to validate or disqualify the delamination hy-
717 pothesis. In this regard, Mongolia is an ideal natural laboratory for studying such intraplate
718 uplift thanks to its location far into the continental interior. It requires crust-mantle interac-
719 tions to explain observations of intracontinental surface deformation far from tectonic plate
720 boundaries where deformation solely by means of plate tectonics is not possible.

721 **ACKNOWLEDGEMENT**

722 This project was financially supported by the SNF (grant No. 200021L_162660/1) and the
723 DFG (grant No. BE5149/6-1) under the DACH program. This work was supported by
724 the Swiss National Supercomputing Center (CSCS) under project ID s828. We thank the
725 Geophysical Instrument Pool Potsdam (GIPP) and the Geothermal Energy and Geofluids

group (Department of Earth Sciences, ETH Zürich) for providing instruments. We thank the field crew and our colleagues from the Mongolian Academy of Science for their support: Batbileg Tegshjargal, Bayrjarga Bizya, Dominic Harpering, Dorian Sörgel, Eldev-Ochir Bold, Friedemann Samrock, Gantsogt Sukhbaatar, Jörg Schmalzl, Nasan-Ochir Tumen, Neeraj Sudhir, Nomuun Narantsogt, Phillip Kotowski, Robin Mann, Sandra Grazioli, Sukhbaatar Usnikh, Tsagaansukh Halzaa, Tserendug Shoovdor, Zagdsuren Shatar and more. We also want to thank Colin Farquharson and one anonymous reviewer for their detailed comments, which helped improve the manuscript significantly.

REFERENCES

- Alzetta, G., Arndt, D., Bangerth, W., Boddu, V., Brands, B., Davydov, D., Gassmüller, R., Heister, T., Heltai, L., Kormann, K., et al., 2018. The deal. II library, version 9.0, *Journal of Numerical Mathematics*, **26**(4), 173–183.
- Ancuta, L. D., Zeitler, P. K., Idleman, B. D., & Jordan, B. T., 2018. Whole-rock $^{40}\text{Ar}/^{39}\text{Ar}$ geochronology, geochemistry, and stratigraphy of intraplate Cenozoic volcanic rocks, central Mongolia, *Bulletin*, **130**(7-8), 1397–1408.
- Aster, R. C., Borchers, B., & Thurber, C. H., 2018. *Parameter estimation and inverse problems*, Elsevier.
- Badarch, G., Cunningham, W. D., & Windley, B. F., 2002. A new terrane subdivision for Mongolia: implications for the Phanerozoic crustal growth of Central Asia, *Journal of Asian Earth Sciences*, **21**(1), 87–110.
- Balay, S., Abhyankar, S., Adams, M. F., Brown, J., Brune, P., Buschelman, K., Dalcin, L., Dener, A., Eijkhout, V., Gropp, W. D., Kaushik, D., Knepley, M. G., May, D. A., McInnes, L. C., Mills, R. T., Munson, T., Rupp, K., Sanan, P., Smith, B. F., Zampini, S., Zhang, H., & Zhang, H., 2018. PETSc users manual, Tech. Rep. ANL-95/11 - Revision 3.10, Argonne National Laboratory.
- Bao, X., Eaton, D. W., & Guest, B., 2014. Plateau uplift in western Canada caused by lithospheric delamination along a craton edge, *Nature Geoscience*, **7**(11), 830.
- Barry, T., Saunders, A., Kempton, P., Windley, B., Pringle, M., Dorjnamjaa, D., & Saandar, S., 2003. Petrogenesis of Cenozoic basalts from Mongolia: evidence for the role of asthenospheric versus metasomatized lithospheric mantle sources, *Journal of Petrology*, **44**(1), 55–91.
- Batmagnai, E., Samrock, F., Grayver, Alexander, V., Kuvshinov, A., Saar, Martin, O., Demberel, S., Tsegmed, B., Tserendug, S., Purevsuren, D., & Oyuntsetseg, D., 2019. Integrated geoscientific

- 757 exploration for geothermal energy utilization in the Mongolian Hangai, in *EGU General Assembly*
758 *Conference Abstracts*, Vienna, Austria.
- 759 Berdichevsky, M., Vanyan, L., Kuznetsov, V., Levadny, V., Mandelbaum, M., Nechaeva, G., Oku-
760 lessky, B., Shilovsky, P., & Shpak, I., 1980. Geoelectrical model of the Baikal region, *Physics of*
761 *the Earth and Planetary Interiors*, **22**(1), 1 – 11.
- 762 Bertrand, E., Caldwell, T., Hill, G., Wallin, E., Bennie, S., Cozens, N., Onacha, S., Ryan, G.,
763 Walter, C., Zaino, A., et al., 2012. Magnetotelluric imaging of upper-crustal convection plumes
764 beneath the Taupo Volcanic Zone, New Zealand, *Geophysical Research Letters*, **39**(2).
- 765 Bird, P., 1979. Continental delamination and the Colorado Plateau, *Journal of Geophysical Re-*
766 *search: Solid Earth*, **84**(B13), 7561–7571.
- 767 Booker, J. R., 2014. The magnetotelluric phase tensor: A critical review, *Surveys in Geophysics*,
768 **35**(1), 7–40.
- 769 Buchan, C., Cunningham, D., Windley, B. F., & Tomurhuu, D., 2001. Structural and lithological
770 characteristics of the Bayankhongor Ophiolite Zone, Central Mongolia, *Journal of the Geological*
771 *Society*, **158**(3), 445–460.
- 772 Cagniard, L., 1953. Basic theory of the magneto-telluric method of geophysical prospecting,
773 *Geophysics*, **18**(3), 605–635.
- 774 Calais, E., Vergnolle, M., San’Kov, V., Likhnev, A., Miroshnitchenko, A., Amarjargal, S., &
775 Déverchère, J., 2003. GPS measurements of crustal deformation in the Baikal-Mongolia area
776 (1994–2002): Implications for current kinematics of Asia, *Journal of Geophysical Research: Solid*
777 *Earth*, **108**(B10).
- 778 Campaña, J., Ledo, J., Queralt, P., Marcuello, A., & Jones, A. G., 2014. A new methodology
779 to estimate magnetotelluric (MT) tensor relationships: Estimation of Local transfer-functions
780 by Combining Interstation Transfer-functions (ELICIT), *Geophysical Journal International*,
781 **198**(1), 484–494.
- 782 Cashman, K. V. & Sparks, R. S. J., 2013. How volcanoes work: A 25 year perspective, *GSA*
783 *bulletin*, **125**(5-6), 664–690.
- 784 Chen, M., Niu, F., Liu, Q., & Tromp, J., 2015. Mantle-driven uplift of Hangai Dome: New seismic
785 constraints from adjoint tomography, *Geophysical Research Letters*, **42**(17), 6967–6974.
- 786 Cherevatova, M., Smirnov, M. Y., Korja, T., Pedersen, L. B., Ebbing, J., Gradmann, S., Becken,
787 M., Group, M. W., et al., 2015. Electrical conductivity structure of north-west Fennoscandia
788 from three-dimensional inversion of magnetotelluric data, *Tectonophysics*, **653**, 20–32.
- 789 Comeau, M., 2015. *Electrical Resistivity Structure of the Altiplano-Puna Magma Body and Volcan*
790 *Uturuncu from Magnetotelluric Data: University of Alberta*, Ph.D. thesis, PhD thesis published
791 by The University of Alberta Education and Research Archive, 337 pp.

- 792 Comeau, M. J., Unsworth, M. J., & Cordell, D., 2016. New constraints on the magma distri-
793 bution and composition beneath Volcán Uturuncu and the southern Bolivian Altiplano from
794 magnetotelluric data, *Geosphere*, **12**(5), 1391–1421.
- 795 Comeau, M. J., Becken, M., Käüfl, J., Kuvshinov, A., Demberel, S., & the Hangai Working Group,
796 2018a. Images of intraplate volcanism: The upper crustal structure below Tariat volcanic zone,
797 Mongolia, imaged with magnetotellurics, in *EGU General Assembly Conference Abstracts*, Vi-
798 enna, Austria.
- 799 Comeau, M. J., Käüfl, J., Becken, M., Kuvshinov, A., Grayver, A., Kamm, J., Demberel, S.,
800 Batmagnai, E., Tserendug, S., Eldev-Ochir, B., & Nasan-Ochir, T., 2018b. Electrical resistivity
801 models reveal mineralization and fault systems in the Valley of the Lakes, south-central Mongolia,
802 in *24th EM Induction Workshop Abstracts*, Helsingør, Denmark.
- 803 Comeau, M. J., Käüfl, J. S., Becken, M., Kuvshinov, A., Grayver, A. V., Kamm, J., Demberel, S.,
804 Sukhbaatar, U., & Batmagnai, E., 2018c. Evidence for fluid and melt generation in response to
805 an asthenospheric upwelling beneath the Hangai Dome, Mongolia, *Earth and Planetary Science*
806 *Letters*, **487**, 201 – 209.
- 807 Comeau, M. J., Becken, M., Käüfl, J., Grayver, A., Kuvshinov, A., Tserendug, S., Batmagnai,
808 E., & Demberel, S., 2019. Evidence for terrane boundaries and suture zones across Southern
809 Mongolia detected with a 2-dimensional magnetotelluric transect, *Earth and Planetary Science*
810 *Letters*, in revision.
- 811 Connolly, J. & Podladchikov, Y. Y., 2013. A hydromechanical model for lower crustal fluid flow,
812 in *Metasomatism and the chemical transformation of rock*, pp. 599–658, Springer.
- 813 Connolly, J. A. D. & Podladchikov, Y. Y., 2004. Fluid flow in compressive tectonic settings: Im-
814 plications for midcrustal seismic reflectors and downward fluid migration, *Journal of Geophysical*
815 *Research: Solid Earth*, **109**(B4).
- 816 Cunningham, W., 2001. Cenozoic normal faulting and regional doming in the southern Hangay
817 region, Central Mongolia: implications for the origin of the Baikal rift province, *Tectonophysics*,
818 **331**(4), 389–411.
- 819 Dmitriev, V. I., Il'inskii, A. S., & Sveshnikov, A. G., 1976. The developments of mathematical
820 methods for the study of direct and inverse problems in electrodynamics, *Russian Mathematical*
821 *Surveys*, **31**(6), 133.
- 822 Dong, H., Wei, W., Jin, S., Ye, G., Zhang, L., Jing, J., Yin, Y., Xie, C., & Jones, A. G., 2016.
823 Extensional extrusion: Insights into south-eastward expansion of Tibetan Plateau from magne-
824 totelluric array data, *Earth and Planetary Science Letters*, **454**, 78 – 85.
- 825 Egbert, G. D., 2002. Processing and interpretation of electromagnetic induction array data,
826 *Surveys in geophysics*, **23**(2-3), 207–249.

- 827 Egbert, G. D. & Booker, J. R., 1986. Robust estimation of geomagnetic transfer functions,
828 *Geophysical Journal of the Royal Astronomical Society*, **87**(1), 173–194.
- 829 Ganbat, E. & Demberel, O., 2010. Geologic background of the Hangay geothermal system, west-
830 central Mongolia, in *Proceedings World Geothermal Congress*, p. 1e6.
- 831 García, X. & Jones, A. G., 2005. A new methodology for the acquisition and processing of
832 audio-magnetotelluric (AMT) data in the AMT dead band, *Geophysics*, **70**(5), G119–G126.
- 833 Grayver, A. V., 2015. Parallel three-dimensional magnetotelluric inversion using adaptive finite-
834 element method. Part I: theory and synthetic study, *Geophysical Journal International*, **202**(1),
835 584–603.
- 836 Grayver, A. V. & Kolev, T. V., 2015. Large-scale 3D geoelectromagnetic modeling using parallel
837 adaptive high-order finite element method, *Geophysics*, **80**(6), E277–E291.
- 838 Grayver, A. V. & Kuvshinov, A. V., 2016. Exploring equivalence domain in nonlinear inverse
839 problems using covariance matrix adaption evolution strategy (CMAES) and random sampling,
840 *Geophysical Journal International*, **205**(2), 971–987.
- 841 Guy, A., Schulmann, K., Janoušek, V., Štípská, P., Armstrong, R., Belousova, E., Dolgoplova,
842 A., Seltmann, R., Lexa, O., Jiang, Y., et al., 2015. Geophysical and geochemical nature of
843 re-laminated arc-derived lower crust underneath oceanic domain in southern Mongolia, *Tectonics*,
844 **34**(5), 1030–1053.
- 845 Harpering, D., 2018. *Robust processing scheme for magnetotelluric data*, Master’s thesis, WWU
846 Münster.
- 847 Harris, N., Hunt, A., Parkinson, I., Tindle, A., Yondon, M., & Hammond, S., 2010. Tectonic im-
848 plications of garnet-bearing mantle xenoliths exhumed by Quaternary magmatism in the Hangay
849 dome, central Mongolia, *Contributions to Mineralogy and Petrology*, **160**(1), 67–81.
- 850 Heise, W., Bibby, H. M., Caldwell, T. G., Bannister, S. C., Ogawa, Y., Takakura, S., & Uchida,
851 T., 2007. Melt distribution beneath a young continental rift: the Taupo Volcanic Zone, New
852 Zealand, *Geophysical Research Letters*, **34**(14).
- 853 Hermance, J. F. & Thayer, R. E., 1975. The telluric-magnetotelluric method, *Geophysics*, **40**(4),
854 664–668.
- 855 Hill, G. J., Bibby, H. M., Ogawa, Y., Wallin, E. L., Bennie, S. L., Caldwell, T. G., Keys, H.,
856 Bertrand, E. A., & Heise, W., 2015. Structure of the Tongariro Volcanic system: Insights from
857 magnetotelluric imaging, *Earth and Planetary Science Letters*, **432**, 115–125.
- 858 Hunt, A. C., Parkinson, I., Harris, N., Barry, T., Rogers, N., & Yondon, M., 2012. Cenozoic vol-
859 canism on the Hangai Dome, Central Mongolia: geochemical evidence for changing melt sources
860 and implications for mechanisms of melting, *Journal of Petrology*, **53**(9), 1913–1942.
- 861 Iliceto, V. & Santarato, G., 1986. On the possibility of the telluric method: some results on faulted

- 862 structures, *Geophysical prospecting*, **34**(7), 1082–1098.
- 863 Ionov, D., 2002. Mantle structure and rifting processes in the Baikal–Mongolia region: geophysical
864 data and evidence from xenoliths in volcanic rocks, *Tectonophysics*, **351**(1-2), 41–60.
- 865 Joshi, A., Bangerth, W., & Sevick-Muraca, E. M., 2004. Adaptive finite element based tomography
866 for fluorescence optical imaging in tissue, *Optics Express*, **12**(22), 5402–5417.
- 867 Karypis, G. & Kumar, V., 1999. A fast and highly quality multilevel scheme for partitioning
868 irregular graphs, *Journal on Scientific Computing*, **20**(1), 359–392.
- 869 Käüfl, J. S., Grayver, A. V., & Kuvshinov, A. V., 2018. Topographic distortions of magnetotelluric
870 transfer functions: a high-resolution 3-d modelling study using real elevation data, *Geophysical
871 Journal International*, **215**(3), 1943–1961.
- 872 Kay, R. W. & Kay, S. M., 1993. Delamination and delamination magmatism, *Tectonophysics*,
873 **219**(1-3), 177–189.
- 874 Khoza, T. D., Jones, A. G., Muller, M. R., Evans, R. L., Miensopust, M. P., & Webb, S. J., 2013.
875 Lithospheric structure of an Archean craton and adjacent mobile belt revealed from 2-D and 3-D
876 inversion of magnetotelluric data: Example from southern Congo craton in northern Namibia,
877 *Journal of Geophysical Research: Solid Earth*, **118**(8), 4378–4397.
- 878 Krystopowicz, N. J. & Currie, C. A., 2013. Crustal eclogitization and lithosphere delamination
879 in orogens, *Earth and Planetary Science Letters*, **361**, 195–207.
- 880 Liu, L. & Hasterok, D., 2016. High-resolution lithosphere viscosity and dynamics revealed by
881 magnetotelluric imaging, *Science*, **353**(6307), 1515–1519.
- 882 Manning, C. E., 2018. Fluids of the lower crust: deep is different, *Annual Review of Earth and
883 Planetary Sciences*, **46**, 67–97.
- 884 McDannell, K. T., Zeitler, P. K., & Idleman, B. D., 2018. Relict topography within the Hangay
885 Mountains in central Mongolia: Quantifying long-term exhumation and relief change in an old
886 landscape, *Tectonics*, **37**(8), 2531–2558.
- 887 Meissner, R. & Mooney, W., 1998. Weakness of the lower continental crust: a condition for
888 delamination, uplift, and escape, *Tectonophysics*, **296**(1-2), 47–60.
- 889 Melosh, G., Cumming, W., Benoit, D., Wilmarth, M., Colvin, A., Winick, J., Soto-Neira, E.,
890 Sussman, D., Urzúa-Monsalve, L., Powell, T., et al., 2010. Exploration results and resource
891 conceptual model of the Tolhuaca geothermal field, Chile, in *Proceedings, World Geothermal
892 Congress*.
- 893 Meltzer, A., Stachnik, J. C., Sodnomsambuu, D., Munkhuu, U., Tsagaan, B., Dashdondog, M., &
894 Russo, R., 2019. The Central Mongolia Seismic Experiment: Multiple Applications of Temporary
895 Broadband Seismic Arrays, *Seismological Research Letters*, **90**(3), 1364–1376.
- 896 Meqbel, N. M., Egbert, G. D., Wannamaker, P. E., Kelbert, A., & Schultz, A., 2014. Deep

- 897 electrical resistivity structure of the northwestern US derived from 3-D inversion of USArray
 898 magnetotelluric data, *Earth and Planetary Science Letters*, **402**, 290–304.
- 899 Miensopust, M. P., 2017. Application of 3-D electromagnetic inversion in practice: Challenges,
 900 pitfalls and solution approaches, *Surveys in Geophysics*, **38**(5), 869–933.
- 901 Muñoz, G., 2014. Exploring for geothermal resources with electromagnetic methods, *Surveys in*
 902 *geophysics*, **35**(1), 101–122.
- 903 Murphy, B. S. & Egbert, G. D., 2017. Electrical conductivity structure of southeastern North
 904 America: implications for lithospheric architecture and Appalachian topographic rejuvenation,
 905 *Earth and Planetary Science Letters*, **462**, 66–75.
- 906 NASA JPL, 2013. NASA Shuttle Radar Topography Mission Global 1 arc second. NASA LP
 907 DAAC, <https://doi.org/10.5067/MEaSURES/SRTM/SRTMGL1.003>.
- 908 Nieuwenhuis, G., Unsworth, M. J., Pana, D., Craven, J., & Bertrand, E., 2014. Three-dimensional
 909 resistivity structure of Southern Alberta, Canada: implications for Precambrian tectonics, *Geo-*
 910 *physical Journal International*, **197**(2), 838–859.
- 911 Oyuntsetseg, D., Ganchimeg, D., Minjigmaa, A., Ueda, A., & Kusakabe, M., 2015. Isotopic and
 912 chemical studies of hot and cold springs in western part of Khangai Mountain region, Mongolia,
 913 for geothermal exploration, *Geothermics*, **53**, 488–497.
- 914 Peacock, J. R., Mangan, M. T., McPhee, D., & Wannamaker, P. E., 2016. Three-dimensional
 915 electrical resistivity model of the hydrothermal system in Long Valley Caldera, California, from
 916 magnetotellurics, *Geophysical Research Letters*, **43**(15), 7953–7962.
- 917 Petit, C., Tiberi, C., Deschamps, A., & Déverchère, J., 2008. Teleseismic traveltimes, topography
 918 and the lithospheric structure across central Mongolia, *Geophysical Research Letters*, **35**(11).
- 919 Platz, A. & Weckmann, U., 2019. An automated new pre-selection tool for noisy Magnetotel-
 920 luric data using the Mahalanobis distance and magnetic field constraints, *Geophysical Journal*
 921 *International*.
- 922 Priestley, K., Debayle, E., McKenzie, D., & Pilidou, S., 2006. Upper mantle structure of eastern
 923 Asia from multimode surface waveform tomography, *Journal of Geophysical Research: Solid*
 924 *Earth*, **111**(B10).
- 925 Rikitake, T., 1948. Notes on electromagnetic induction within the Earth, *Bull. Earthq. Res. Inst.*,
 926 **24**(1), 4.
- 927 Rizza, M., Ritz, J.-F., Prentice, C., Vassallo, R., Braucher, R., Larroque, C., Arzhannikova, A.,
 928 Arzhannikov, S., Mahan, S., Massault, M., et al., 2015. Earthquake geology of the Bulnay fault
 929 (Mongolia), *Bulletin of the Seismological Society of America*, **105**(1), 72–93.
- 930 Robertson, K., Heinson, G., & Thiel, S., 2016. Lithospheric reworking at the Proterozoic-
 931 Phanerozoic transition of Australia imaged using AusLAMP Magnetotelluric data, *Earth and*

- 932 *Planetary Science Letters*, **452**, 27 – 35.
- 933 Robertson, K., Heinson, G., Taylor, D., & Thiel, S., 2017. The lithospheric transition between
934 the Delamerian and Lachlan orogens in western Victoria: new insights from 3D magnetotelluric
935 imaging, *Australian Journal of Earth Sciences*, **64**(3), 385–399.
- 936 Rousseeuw, P. J., 1984. Least median of squares regression, *Journal of the American Statistical*
937 *Association*, **79**(388), 871–880.
- 938 Rung-Arunwan, T., Siripunvaraporn, W., & Utada, H., 2016. On the Berdichevsky average,
939 *Physics of the Earth and Planetary Interiors*, **253**, 1 – 4.
- 940 Sahagian, D., Proussevitch, A., Ancuta, L., Idleman, B., & Zeitler, P., 2016. Uplift of Central
941 Mongolia recorded in vesicular basalts, *The Journal of Geology*, **124**(4), 435–445.
- 942 Samrock, F., Grayver, A. V., Eysteinnsson, H., & Saar, M. O., 2018. Magnetotelluric image of
943 transcrustal magmatic system beneath the Tulu Moye geothermal prospect in the Ethiopian rift,
944 *Geophysical Research Letters*, **45**(23), 12–847.
- 945 Styron, R., 2018. GEM global active faults, <http://doi.org/10.5281/zenodo.1404388>.
- 946 Tiberi, C., Deschamps, A., Déverchère, J., Petit, C., Perrot, J., Appriou, D., Mordvinova, V.,
947 Dugaarma, T., Ulzibaat, M., & Artemiev, A., 2008. Asthenospheric imprints on the lithosphere in
948 central Mongolia and southern Siberia from a joint inversion of gravity and seismology (MOBAL
949 experiment), *Geophysical Journal International*, **175**(3), 1283–1297.
- 950 Tietze, K. & Ritter, O., 2013. Three-dimensional magnetotelluric inversion in practice—the electri-
951 cal conductivity structure of the San Andreas Fault in Central California, *Geophysical Journal*
952 *International*, **195**(1), 130–147.
- 953 Tikhonov, A., 1950. On determining electrical characteristics of the deep layers of the Earth's
954 crust, in *Doklady*, vol. 73, pp. 295–297, Citeseer.
- 955 Tikhonov, A. N., 1963. On the solution of ill-posed problems and the method of regularization,
956 in *Doklady Akademii Nauk*, vol. 151, pp. 501–504, Russian Academy of Sciences.
- 957 Unsworth, M. & Bedrosian, P. A., 2004. Electrical resistivity structure at the SAFOD site from
958 magnetotelluric exploration, *Geophysical Research Letters*, **31**(12).
- 959 Usui, Y., Ogawa, Y., Aizawa, K., Kanda, W., Hashimoto, T., Koyama, T., Yamaya, Y., &
960 Kagiya, T., 2016. Three-dimensional resistivity structure of Asama volcano revealed by data-
961 space magnetotelluric inversion using unstructured tetrahedral elements, *Geophysical Journal*
962 *International*, **208**(3), 1359–1372.
- 963 Van der Voo, R., van Hinsbergen, D. J., Domeier, M., Spakman, W., & Torsvik, T. H., 2015.
964 Latest Jurassic–earliest Cretaceous closure of the Mongol–Okhotsk Ocean: A paleomagnetic and
965 seismological–tomographic analysis, *Geological Society of America Special Papers*, **513**, 589–606.
- 966 Vergnolle, M., Pollitz, F., & Calais, E., 2003. Constraints on the viscosity of the continental crust

- 967 and mantle from GPS measurements and postseismic deformation models in western Mongolia,
968 *Journal of Geophysical Research: Solid Earth*, **108**(B10).
- 969 Walker, R., Nissen, E., Molor, E., & Bayasgalan, A., 2007. Reinterpretation of the active faulting
970 in central Mongolia, *Geology*, **35**(8), 759–762.
- 971 Walker, R., Molor, E., Fox, M., & Bayasgalan, A., 2008. Active tectonics of an apparently aseis-
972 mic region: distributed active strike-slip faulting in the Hangay Mountains of central Mongolia,
973 *Geophysical Journal International*, **174**(3), 1121–1137.
- 974 Weidelt, P., 1972. The inverse problem of geomagnetic induction, *J. Geophys.*, **38**, 257–289.
- 975 Windley, B. F. & Allen, M. B., 1993. Mongolian plateau: Evidence for a late Cenozoic mantle
976 plume under central Asia, *Geology*, **21**(4), 295–298.
- 977 Xu, S., Unsworth, M. J., Hu, X., & Mooney, W. D., 2019. Magnetotelluric evidence for asym-
978 metric simple shear extension and lithospheric thinning in south China, *Journal of Geophysical*
979 *Research: Solid Earth*, **124**(1), 104–124.
- 980 Yang, B., Egbert, G. D., Kelbert, A., & Meqbel, N. M., 2015. Three-dimensional electrical
981 resistivity of the north-central USA from EarthScope long period magnetotelluric data, *Earth*
982 *and Planetary Science Letters*, **422**, 87 – 93.
- 983 Yoshino, T., Matsuzaki, T., Shatskiy, A., & Katsura, T., 2009. The effect of water on the electrical
984 conductivity of olivine aggregates and its implications for the electrical structure of the upper
985 mantle, *Earth and Planetary Science Letters*, **288**(1), 291 – 300.
- 986 Yungul, S. H., 1977. The telluric methods in the study of sedimentary structures-a survey, *Geo-*
987 *exploration*, **15**(4), 207–238.
- 988 Zhang, F., Wu, Q., Grand, S. P., Li, Y., Gao, M., Demberel, S., Ulziibat, M., & Sukhbaatar, U.,
989 2017. Seismic velocity variations beneath central Mongolia: Evidence for upper mantle plumes?,
990 *Earth and Planetary Science Letters*, **459**, 406–416.